

**Chip-scale Photonic Devices for Light-matter
Interactions and Quantum Information
Processing**

Jie Gao

Submitted in partial fulfillment of the
requirements for the degree
of Doctor of Philosophy
in the Graduate School of Arts and Sciences

COLUMBIA UNIVERSITY

2012

© 2011

Jie Gao

All Rights Reserved

ABSTRACT

Chip-scale Photonic Devices for Light-matter Interactions and Quantum Information Processing

Jie Gao

Chip-scale photonic devices such as microdisks, photonic crystal cavities and slow-light photonic crystal waveguides possess strong light localization and long photon lifetime, which will significantly enhance the light-matter interactions and can be used to implement new functionalities for both classical and quantum information processing, optical computation and optical communication in integrated nanophotonic circuits. This thesis will focus on three topics about light-matter interactions and quantum information processing with chip-scale photonic devices, including 1) Design and characterization of asymmetric resonant cavity with radiation directionality and air-slot photonic crystal cavity with ultrasmall effective mode volume, 2) Exciton-photon interactions between quantum dots and photonic crystal devices and non-classical photon source from a single quantum dot, and 3) Quantum

controlled phase gate and phase switching based on quantum dots and photonic crystal waveguide.

The first topic is engineered control of radiation directionality and effective mode volume for optical mode in chip-scale silicon micro-/nano-cavities. High quality factor (Q), subwavelength mode volume (V) and controllable radiation directionality are the major properties for optical cavities designs. In Chapter 2, asymmetric resonant cavities with rational caustics are proposed and interior whispering gallery modes in monolithic silicon mesoscopic microcavities are experimentally demonstrated. These microcavities possess unique robustness of cavity quality factor against roughness Rayleigh scattering. In Chapter 3, air-slot mode-gap photonic crystal cavities with quality factor of 10^4 and effective mode volume ~ 0.02 cubic wavelengths are experimentally demonstrated. The origin of the high Q air-slot cavity mode is the mode-gap effect from the slotted photonic crystal waveguide mode with negative dispersion.

The second topic is exciton-photon coupling between quantum dots and two-dimensional photonic crystal nanocavities and waveguide localized modes, including Purcell effect in weak coupling regime and vacuum Rabi splitting in strong coupling regime. In Chapter 4, micro-photoluminescence measurements of PbS quantum dots coupled to air-slot mode-gap photonic crystal cavities with potentially high quality factor and small effective mode volume are presented. Purcell factor due to ultrahigh Q/V ratios are critical for applications in non-classical photon sources, cavity QED, nonlinear optics and sensing. In Chapter 5, the observation of subpoisson photon

statistics from a single InAs quantum dot emission is presented from both continuous wave and pulsed Hanbury Brown and Twiss measurement. Furthermore, strong coupling between single quantum dot exciton line and photonic crystal waveguide localized mode is demonstrated experimentally and theoretically analyzed with master equations, which can be used as a great implementation platform for realizing future solid-state quantum computation.

The third topic is quantum controlled phase gate and phase switching operations based on quantum dots and photonic crystal slow-light waveguide. In Chapter 6, we propose a scheme to realize controlled phase gate between two single photons through a single quantum dot embedded in a photonic crystal waveguide. Enhanced Purcell factor and large β factor lead to high gate fidelity over broadband frequencies compared to cavity-assisted system. The excellent physical integration of this photonic crystal waveguide system provides tremendous potential for large-scale quantum information processing. In Chapter 7, dipole induced transparency can be achieved in a system which consists of two quantum dots properly located in silicon photonic crystal waveguide. Furthermore, we describe how this effect can be useful for designing full π phase switching in a hetero-photonic crystal waveguide structure just by a small amount of photons.

Contents

List of Figures	iv
Acknowledgements	x
Chapter 1: Introduction	1
1.1 Chip-scale photonic devices for light-matter interactions and quantum information processing	2
1.2 Thesis organization	5
Bibliography	8
Chapter 2: Interior whispering gallery modes in asymmetric resonant cavities (ARCs) with directional emission	11
2.1 Introduction	12
2.2 Design of ARCs with interior whispering gallery modes (IWG)	13
2.3 Nanofabrication of silicon ARCs	15
2.4 Experimental demonstration of IWG modes with directional emission	15
2.4.1 Angled-resolved tapered fiber transmission measurement	16
2.4.2 Near-infrared imaging of modes radiation	18
2.5 Conclusion	19
Bibliography	25
Chapter 3: Air-slot mode-gap confined photonic crystal (PhC) slab cavities with ultrasmall effective mode volume	27

3.1 Introduction	28
3.2 Design and characterization of air-slot L3 cavity	29
3.3 Design of air-slot PhC cavities with high Q and ultras-small V_{eff}	31
3.4 Experimental setup and characterization for air-slot mode-gap PhC cavities	33
3.5 Conclusion	35
Bibliography	45
Chapter 4: Weak exciton-photon coupling between ensemble PbS Quantum dots and air-slot mode-gap photonic crystal cavities	47
4.1 Introduction	48
4.2 Device preparation and micro-photoluminescence measurement	49
4.3 Polarization and power dependent analysis	50
4.4 Conclusion	52
Bibliography	56
Chapter 5: Strong exciton-photon coupling between single InAs Quantum dot and GaAs photonic crystal waveguide localized mode	57
5.1 Introduction	58
5.2 Optical characterization for a single quantum dot (QD)	59
5.2.1 Single QD imaging and spectroscopy	59
5.2.2 Hanbury Brown-Twiss (HBT) measurement	61
5.3 GaAs photonic crystal waveguide localized mode	62
5.4 Experiment and theoretical analysis of strong exciton-photon coupling	63
5.5 Conclusion	66
Bibliography	74
Chapter 6: Quantum controlled phase gate through a single quantum dot in a slow-light photonic crystal waveguide	76
6.1 Introduction	77

6.2 Transport property for PhC waveguide embedded with a single QD	78
6.3 Construction scheme for quantum controlled phase gate	81
6.4 Gate fidelity and photon loss analysis	83
6.5 Conclusion	87
Bibliography	90
Chapter 7: Phase switching through two quantum dots in a slow-light photonic crystal waveguide	92
7.1 Introduction	93
7.2 Transport property for PhC waveguide embedded with two QDs	93
7.3 Construction schemes for full π phase switching	96
7.5 Conclusion	99
Bibliography	104
Chapter 8: Summary and future outlook	105
8.1 Summary	106
8.2 Future outlook	107
Bibliography	109

List of Figures

- 2.1** (a) Poincaré surface of section plot. Horizontal axis ϕ represents the intercept point of the ray and the cavity boundary, and vertical axis θ represents the incident angle between the ray and the tangent line of the boundary. The red solid line corresponds to the total internal reflection. (b) IWG mode supported near the rational caustic and (c) the fundamental WGM mode. (d) Numerical simulations of Q_s for WGMs (squares) and IWG modes (circles) versus cavity edge roughness. **20**
- 2.2** Experimental setup of tapered fiber characterization measurement. Light from ASE source, passing through an in-line fiber polarizer and a polarization controller, is evanescently coupled into cavity through tapered fiber. Fiber transmissions are monitored on optical spectrum analyzer to observe cavity resonances, and vertical radiations from the top of ARCs are captured by near-infrared camera. **21**
- 2.3** (a) Normalized transmission spectra when the taper touches the resonator side in tangential direction at different positions. (b) SEM of fabricated suspended silicon ARC on oxide pedestal. Dotted lines (--) show tapered fiber spatial probe positions [(1) - (4)]. (c) Transmission spectrum for TE-like and TM-like polarization. **22**
- 2.4** (a) Normalized transmission spectra when the taper is positioned along different coupling angle θ at position (3). (b) Experimental and numerical (inset) results for coupling depth versus θ . (c) Near-field images of IWG modes (c2) and WGMs (c1). **23**

- 2.5** (a) Transmission spectrum when fiber-cavity separation $g = 0$. (b) Coupling depth (circles) and Q factor (squares) as functions of g . Inset: Experiment illustration for measuring the Q value. **24**
- 3.1** (a) E_x field intensity of L3 cavity in the x - y plane. (b) E_x field intensity of air slot cavity in the x - y plane. (c) Squared electric field distribution (black: L3 cavity; red: Slot cavity) along x direction ($y=0, z=0$). **37**
- 3.2** (a) SEM of the fabricated cavity with an air slot. Scale bar: $1\mu\text{m}$. (b) E_x field intensity of localized mode calculated from FDTD simulation using the fabricated parameters. (c) TE band structure of silicon air-bridged 2D photonic crystal slab. Blue line indicates the localized mode shown in (b). **38**
- 3.3** (a) Optical micrograph of the tapered fiber aligned along the y axis of the cavity. (b) Normalized taper transmissions for devices with different air hole radius when the taper touches the cavity. (c) Normalized taper transmission when the input light is TE-polarized (red) and TM-polarized (black). **39**
- 3.4** (Left) Normalized taper transmissions as a function of fiber-cavity gap. (Right) Full widths at the half maximum of the mode as a function of the gap. **40**
- 3.5** (a) Band structure of slotted W1 PhCWG with $a = 490\text{nm}$, $r = 0.34a$, $t = 0.449a$, $n_{\text{si}}=3.48$ and slot width $s=80\text{nm}$. (b-I,II,III) Field distributions (Left: H_z ; Right: $|E|^2$) of the three modes inside TE band gap. **41**
- 3.6** (a-c) 2D FDTD simulation of $|E|^2$ spatial distribution and the $|E|^2$ value across the air slot for cavity modes created from photonic waveguide mode I, II, III respectively. **42**

- 3.7** (a) SEM of the air-slot mode-gap confined cavity. (b-c) 3D FDTD simulation and Fourier transform of the electric field for cavity mode due to mode-gap effect of waveguide mode I. **43**
- 3.8** (a) SEM of the air-slot mode-gap confined cavity with in-line coupling waveguide. The base width of a line defect $W_0 = \sqrt{3}a$ and the width of input/output waveguides is $W_c = 1.05 \times \sqrt{3}a$. The distance between the cavity and coupling waveguide is $L_c = 4.5a$. Red circle indicates the region from which the radiation signals are collected. (b-d) Radiation spectra of three devices: (b) $W_0 = \sqrt{3}a$, $s = 80\text{nm}$ and $r = 0.306$; (c) $W_0 = \sqrt{3}a$, $s = 80\text{nm}$ and $r = 0.285$; (d) $W_0 = 1.2 \times \sqrt{3}a$, $s = 120\text{nm}$ and $r = 0.285$. **44**
- 4.1** (a) SEM picture of the air-slot mode-gap confined cavity with PbS QDs on the surface. The red highlighted region shows the non-uniform QD distribution, and even single PbS QD can be seen clearly. (b) PL spectra of three devices: (blue) $W_0 = 1.2 \times \sqrt{3}a$, $s = 120\text{nm}$ and $r = 0.296a$; (red) $W_0 = \sqrt{3}a$, $s = 80\text{nm}$ and $r = 0.31a$; (black) $W_0 = 1.2 \times \sqrt{3}a$, $s = 100\text{nm}$ and $r = 0.324a$. (c) Zoom in and Lorentzian fit of the blue PL spectrum in (b). The inset shows the inhomogeneous PL spectrum from ensemble PbS QDs. **53**
- 4.2** (a) PL spectra for TE_x (grey) and TE_y (red) polarization of a particular device in which two resonances are observed. (b) Magnetic field H_z distribution for mode II in air-slot mode-gap cavity. (c) Magnetic field H_z and electric field energy distribution $|E|$ for mode II in air-slot photonic crystal waveguide. **54**
- 4.3** Power saturation measurements for QDs coupled to waveguide mode (black), to cavity mode (red) and uncoupled QDs (green). Dashed lines are linear fits before saturation and arrows indicate the excitation powers at the onset of saturation. **55**

- 5.1** Experiment setup for single quantum dot spectroscopy and HBT measurement. Collection efficiency is 0.8% (-21dB) for spectrum and 0.2% (-27dB) for correlation measurement. **68**
- 5.2** (a-b) Single quantum dot imaging on cooled Si CCD of a sample with ultralow QD density. A single quantum dot can be selected by narrowing the entrance slit of the spectrometer. (c) PL spectrum from a single QD in (b) under very low CW He-Ne excitation. **69**
- 5.3** (a) (b) A single QD exciton line spectrum and HBT measurement under cw laser excitation at 9K. The normalized coincidence counts at time interval zero is ~ 0.5 . (c) (d) A single QD exciton line spectrum and HBT measurement under pulsed laser excitation. The normalized coincidence counts at time interval zero is ~ 0.28 . **70**
- 5.4** (a) A scanning electron microscope (SEM) image of a fabricated PhC waveguide (b) Band structure for PhC waveguide used in experiment. Red and blue lines indicate the high order and fundamental waveguide modes, and the red box shows the slow light region where localized modes are expected. (c) Electric field energy $|E|^2$ (top) and magnetic field H_z (bottom) distributions for high order waveguide mode near slow light region. **71**
- 5.5** (a) Polarization dependence measurements of the QDs and localized mode when $T = 40\text{K}$ with high excitation power $\sim 20\mu\text{W}$. (b) Power dependence measurements of the QDs and localized mode when $T = 20\text{K}$. **72**
- 5.6** (a) Experimental spectra (solid curves) and calculated spectra (open circles) of the coupled system when temperature is scanned from 26K to 29.5K. (b) Resonances of two polariton peaks (red and black dots) extracted from experimental spectra in (a)

vs. temperature. Blue dots and dash lines (linear fits to blue dots) represent uncoupled cavity and QD wavelength increase with temperature in different rates.

73

6.1 (a) PhC waveguide band structure within the TE-like band gap. Both fundamental (red) and a higher order mode (blue) are shown. Structure parameters: $r = 0.275a$, $h = 0.5a$, $\varepsilon = 12$ and $a = 420\text{nm}$. (b) Schematic diagram of a single incident photon interacts with a near resonant QD. (c) Reflectance as a function of normalized quantum dot detuning frequencies for different normalized PhC waveguide frequencies with quantum dot $\tau_{\text{NR}} = 10\tau_0$ and $\tau_{\text{NR}} = \tau_0$. Inset: Reflection coefficient (real part and imaginary part) and phase when $f = 0.2662$, $\tau_{\text{NR}} = 10\tau_0$.

88

6.2 (a) Schematic setup of CPF gate with Sagnac loop. Photon A (B) enters from Port A (B) and the h -polarized component (after passing the PBS) interacts with single quantum dot positioned in the PhC waveguide. (b) Gate photon loss as a function of normalized quantum dot detuning frequencies for CPF gate operated at different PhC waveguide frequencies with quantum dot $\tau_{\text{NR}} = 10\tau_0$ and $\tau_{\text{NR}} = \tau_0$. (c) Gate fidelity for different detuning frequencies and PhC waveguide frequencies ($\tau_{\text{NR}} = 10\tau_0$) (d) CPF gate fidelity as a function of normalized PhC waveguide frequencies with quantum dots $\tau_{\text{NR}} = 10\tau_0$, $\tau_{\text{NR}} = \tau_0$ and $\tau_{\text{NR}} = 0.1\tau_0$.

89

7.1 (a) PhC waveguide band structure within the TE-like band gap. Both fundamental and higher order modes are shown. Structure parameters: $r=0.275a$, $h=0.5a$, $\varepsilon=12$ and $a=420\text{nm}$. (b) Schematic diagram of incident beam interacts with two near resonant QDs. (c) Transmittance (red in upper (c)), Reflectance (blue in upper (c)) and phase of the transmitted beam (bottom (c)) as a function of input frequencies.

$|\omega_A - \omega_B| \cdot \tau_0 = 30$, $\tau_0 = 1\text{ns}$ and distance between two QDs $L = 4a$.

100

7.2 Schematic diagram for full π phase switching based on an in-plane hetero-photonic crystal structure and two three-level QDs. Lattice constants in different photonic crystal region is a_1 and a_2 . The distance between the hetero-interface and quantum dot B is $L/2+d$ and the phase introduced by reflection at the interface is φ , which satisfy $2k \cdot d + \varphi = 2\pi$. **101**

7.3 (a) Reflectance, phase and group delay for $\tau_0 = 1\text{ns}$, $\tau_{\text{NR}} = 10\tau_0$, $|\omega_A - \omega_B| \cdot \tau_0 = 30$, $2k \cdot d + \varphi = 2\pi$ and $L = 4a$. Reflectance and phase when (b) $\tau_{\text{NR}} = 0.5\tau_0$ (c) $|\omega_A - \omega_B| \cdot \tau_0 = 50$ (d) $2k \cdot d + \varphi = 2.2\pi$ (e) $L = 4.02a$. All the other parameters keep the same as (a) for each case. **102**

7.4 Reflection and phase when there is Stark field (red curve) and no Stark field (blue curve). $|\omega_A - \omega_B| \cdot \tau_0 = 20$, $\Delta = 0.4 \text{ THZ}$, $T = 40\text{ps}$ and $N=5$. **103**

Acknowledgements

First my deep appreciation goes to my advisor, Professor Chee Wei Wong, for his grateful support, guidance and encouragement through all the years I have spent in optical nanostructures laboratory. His enthusiasm and passion for research and education have been inspiring me a lot. I really enjoy the coupling and interactions with him all throughout these years. I also want to thank him for providing an active and dynamic research environment for me to interact with all the other great people in the Optical Nanostructures Laboratory.

I would also like to thank Professor Richard Osgood for introducing photonic devices design methods to me during my first semester and Professor Tony Heinz for all the helpful academic career suggestions. There were several courses that help my doctoral research, for example Professor Jim Misewich's "Fundamentals of Photonics" which formed the basis for my research on optics, Professor Dirk Englund's "Applied Quantum Optics" which deeply extended my understanding of the quantum nature of single photons, and Professor Shalom Wind's "Nanofabrication" which helped a lot on solving the fabrication issues I met during my experiment. I greatly appreciate the precision and depth of their teachings on these subjects. I also want to acknowledge other members of my proposal and thesis committee, including Professor Aron Pinczuk and Professor Horst Stormer for their useful comments and suggestions for the work included in this thesis.

All the members in the Optical Nanostructures Laboratory have significantly contributed to this thesis. I would particularly like to thank Xiaodong Yang and Ranjoy Bose, who have taught me the first experiment hand by hand and kindly shared all their research experiences with me. Xiaodong and I have shared so many exciting moments such as for the first time we succeeded to couple a tapered fiber to a

microdisk. Ranojoy and I have experienced so many times together on inspiring and wonderful discussions on the understandings of experiment results. Besides the experimental techniques, I have been able to learn a lot from them on how to conduct a research project by my own.

I also had the pleasure of working closely with another two hardworking and intelligent colleagues James McMillan and Jiangjun Zheng, who was very nice to share their knowledge on lots of equipment and experiment details. I also want to thank all the other current and former members in our group for sharing many things with me. They are Rohit Chatterjee, Kai Liu, Fangwen Sun, Felice Gesuele, Chad Husko, Jing Shu, Charlton Chen, Serdar Kocaman, Ying Li, Tingyi Gu.

This thesis would not have been possible without the help of Professor Diana Hoffman's group at UCLA (Baolai Liang and Adam Scott), Professor Alfredo Derossi's group at Thales (Sylvain Combrie and Gaelle Lehoucq), Dr. Pascal Heider from Columbia APAM, Dr. Steven G. Johnson, members of IME Singapore (Mingbin Yu and Dim-Lee Kwong), Aaron Stein from BNL. I appreciate all the invaluable discussions with them and their contributions to optical simulations, sample growth and device nanofabrication.

In addition, I would also like to thank Professor Guangcan Guo and Professor Zhengfu Han at University of Science and Technology of China, who helped me to enter into optics research area and to explore the beauty of science in the first place during my undergraduate studies.

Finally, I would like to thank my parents and my husband, for their continuous support, unconditional love and all the encouragement through all these years.

Chapter 1

Introduction

1.1 Chip-scale photonic devices for light-matter interactions and quantum information processing

Long photon lifetime and strong photon confinement in chip-scale optical cavities and waveguide [1-3] are critical for a vast span of fundamental studies and applications, ranging from ultra-low threshold microcavity lasers; nonlinear frequency generation [4-5]; dynamic filters and memory for communications; to interactions of atoms with cavity modes in both strong and weak coupling regimes in cavity quantum electrodynamics (QED) [6-7]. Many optical cavities with high quality factor and small mode volume (V) have been developed and fabricated, including Fabry-Perot cavities [8], microspheres [9], silicon and silica whispering gallery type resonators [10-11] and photonic crystal nanocavities [12-13]. Among them, two-dimensional whispering gallery type resonant structures have achieved remarkable Q up to $\sim 10^8$ with $V \sim 450(\lambda/n)^3$ [2]. A desirable characteristic of these planar whispering gallery mode resonators is that of directional emission, without significant Q -spoiling from the loss of rotational symmetry [14-17]. These asymmetric resonant cavities also have potential applications in the study of disorder and localization in mesoscopic systems as well as quantum chaos [18] in the diffusive limit. For devices with much smaller mode volume, two-dimensional silicon photonic crystal cavities have achieved remarkable Q up to $\sim 10^6$ experimentally with mode volume traditionally on the order of the wavelength of light. Further reducing effective mode volume V_{eff} in cavities enables one to control the degree of light-matter interaction for processes such as

nonlinear optics [19] and cavity quantum electrodynamics (QED) [20]. The Purcell factor for an emitter in a resonant cavity is inversely proportional to V_{eff} [21], and the Rabi frequency is inversely proportional to the square root of V_{eff} [22]. By introducing a non-terminated air slot into photonic crystal structures as dielectric discontinuities [23], both high Q and ultrasmall mode volume can be achieved which benefit the study of light matter interactions. For silicon photonic crystal devices working in $1.5\mu\text{m}$ [24-26], colloidal quantum dots (QDs) formed through synthesis in solution such as PbS nanocrystals have emerged as a promising candidate to integrate on those photonic devices. Coupling QDs to photonic structures result in a faster recombination rate for the excitons which helps to overcome decoherence issues in the application of single photon source and cavity QED. In the case of weak coupling, the spontaneous emission rates of the excitons are enhanced by Purcell factor [27].

The study of exciton-photon coupling in chip-scale photonic devices is of central interest in the field of solid-state cavity quantum electrodynamics [28-31]. The coupled system has been examined as a critical component for quantum information processing, including demonstrations of the single photon source [32], strong coupling [33, 34], two-qubit quantum gate operation [35] and entanglement generation [36]. Generally the prototypical system involves a high quality factor and small mode volume optical cavity, providing a platform to achieve strong coherent interactions between the quantum dot and photon. Using a cavity to modify the local density of states, however, it is typically limited to a narrow-band spectral region, in addition to photon extraction, scalability and integration issues that need to be carefully

considered. Alternatively, one-dimensional slow-light photonic crystal waveguides and surface plasmons waveguides can also be used to increase the local density of states for enhanced light-matter interactions such as spontaneous emission enhancement [37], and furthermore to achieve single photon transistors [38], single photon sources [39] and controlled phase gate [40]. Remarkable observations such as spontaneous emission enhancement with ensemble QDs in a photonic crystal waveguide have recently been observed [41]. It makes use of the tight optical confinement and low group velocity of waveguide modes to influence the emission of a QD localized inside the standard photonic crystal waveguide. Moreover, excitation of waveguide mode and extraction of quantum dot emission are extremely efficient in this system, and chip-scale integration is possible. Large optical nonlinearities can be created by dipole induced transparency phenomenon [42] and dispersive properties without high Q cavity assistance. Photonic crystal waveguide, together with quantum dot, has great potential for the applications from “optical transmission line” to “information processing”. Also due to the interference of the coherently scattered light in waveguide devices with unavoidable structural disorder from fabrication, localized modes with high quality factor (Q) have been observed near the slow-light band edge [43, 44]. Recently spontaneous emission control of a single quantum dot (QD) through localization mode (Q up to $\sim 10,000$) in photonic crystal waveguide with engineered disorder has been shown [45]. This photonic crystal waveguide localized mode with a single quantum dot possesses remarkable possibilities towards efficient single photon

sources on-demand and controls light-matter interactions in the strong coupling regime for quantum information science.

1.2 Thesis organization

Chip-scale photonic devices such as microdisks, photonic crystal cavities and slow-light photonic crystal waveguides possess strong light localization and long photon lifetime, which will significantly enhance the light-matter interactions and can be used to implement new functionalities for both classical and quantum information processing, optical computation and optical communication in integrated nanophotonic circuits. This thesis will focus on three topics about light-matter interactions and quantum information processing with chip-scale photonic devices, including design and characterization of asymmetric resonant cavity with radiation directionality and air-slot photonic crystal cavity with ultrasmall effective mode volume (Chapter 2 and 3), exciton-photon interactions between quantum dots and photonic crystal devices and non-classical photon source from a single quantum dot (Chapter 4 and 5), and quantum controlled phase gate and phase switching based on quantum dots and photonic crystal waveguide (Chapter 6 and 7).

In Chapter 2, numerical methods to design remarkable asymmetric resonant cavities with high Q interior whispering gallery modes are proposed. Distinct resonant families and directional radiation from interior whispering gallery modes are observed experimentally using angle-resolved tapered fiber measurements and near-field images. These monolithic silicon mesoscopic microcavities possess unique robustness of

cavity quality factor against roughness Rayleigh scattering, and can be used for microcavity laser and cavity quantum electrodynamics applications.

In Chapter 3, air-slot mode-gap photonic crystal cavities with quality factor of 10^4 and effective mode volume ~ 0.02 cubic wavelengths are experimentally demonstrated. The origin of the high Q air-slot cavity mode is the mode-gap effect from the slotted photonic crystal waveguide mode with negative dispersion. The high Q cavities with ultrasmall mode volume are important for applications such as cavity quantum electrodynamics, nonlinear optics, and optical sensing.

In Chapter 4, we experimentally present weak exciton-photon coupling of PbS quantum dots in air-slot mode-gap cavities which have been demonstrated with high Q and ultra-small mode volume in Chapter 3. Purcell factor due to ultrahigh Q/V ratios are examined through photoluminescence enhancement and the delayed onset saturation power for QDs coupled to cavity mode, which are critical for applications in non-classical photon sources, cavity QED, nonlinear optics and sensing.

In Chapter 5, single photon emission from an InAs quantum dot is measured from single quantum dot spectroscopy and second order photon correlation measurement. Two-dimensional photonic crystal devices coupled with single quantum dot are great candidates for realizing efficient single photon sources and future solid state quantum computation. Strong coupling between single quantum dot exciton line and localized mode in photonic crystal waveguide is demonstrated, which can be used as a great implementation platform to study quantum optics phenomena such as

photon blockade and tunneling, nonlinearity in Jaynes-Cummings ladder and coherent control of quantum polaritons.

In Chapter 6, implementation scheme is proposed to realize quantum controlled phase gate between two single photons through a single quantum dot in a slow-light photonic crystal waveguide. Enhanced Purcell factor and large β factor lead to high gate fidelity over broadband frequencies compared to cavity-assisted system. Single qubit rotation operation and two qubits gate operation are building blocks to quantum computation and quantum information processing. Implementation system based on quantum dots and photonic crystal waveguide is very promising to be a critical component in quantum information processing. The excellent physical integration of this photonic crystal waveguide system provides tremendous potential for large-scale quantum information processing.

In Chapter 7, dipole induced transparency can be achieved in a system which consists of two quantum dots properly located in silicon photonic crystal waveguide. Furthermore, full π phase switching can be performed in a hetero-photonic crystal waveguide structure just by a small amount of photons.

In Chapter 8, we summary all the work in this thesis and propose future look to the field of solid-state cavity electrodynamics and quantum information processing.

Bibliography

- [1] R. K. Chang and A. J. Campillo (editors), *Optical Processes in Microcavities* (Advanced Series in Applied Physics; vol. **3**), World Scientific Publishers, Singapore, 1996.
- [2] K. J. Vahala (editor), *Optical Microcavities* (Advanced Series in Applied Physics; vol. **5**), World Scientific Publishers, Singapore, 2005 ; K. J. Vahala, *Nature* **424**, 839 (2003).
- [3] S. Noda, M. Fujita, and T. Asano, *Nature Photonics* **1**, 449 (2007).
- [4] T. Carmon and K. Vahala, *Nature Physics* **3**, 430 (2007).
- [5] X. Yang and C. W. Wong, *Optics Express* **15**, 4763 (2007).
- [6] T. Aoki, B. Dayan, E. Wilcut, W. P. Bowen, A. S. Parkins, T. J. Kippenberg, K. J. Vahala and J. Kimble, *Nature* **443**, 671 (2006).
- [7] R. Bose, X. Yang, R. Chatterjee, J. Gao, and C. W. Wong, *Appl. Phys. Lett.* **90**, 11117 (2006).
- [8] K. J. Vahala, *Nature* **424**, 839 (2003).
- [9] I. S. Grudinin, A. B. Matsko, and L. Maleki, *Optics Express* **15**, 3390 (2007).
- [10] M. Soltani, S. Yegnanarayanan, and A. Adibi, *Optics Express* **15**, 4694 (2007); S. Xiao, M. H. Khan, H. Shen, and M. Qi, *Optics Express* **15**, 14467 (2007); A. Nitkowski, L. Chen, L., and M. Lipson, *Optics Express* **16**, 11930 (2008); J. Gao, P. Heider, C. J. Chen, X. Yang, C. A. Husko, and C. W. Wong, *Appl. Phys. Lett.* **91**, 181101 (2007).
- [11] D. K. Armani, T. J. Kippenberg, S. M. Spillane and K. J. Vahala, *Nature* **421**, 925 (2003).
- [12] S. Noda, M. Fujita, and T. Asano, *Nature Photonics* **1**, 449 (2007).
- [13] T. Tanabe, M. Notomi, E. Kuramochi, A. Shinya, H. Taniyama, *Nature Photonics* **1**, 49 (2007).
- [14] C. Gmachl, F. Capasso, E. E. Narimanov, J. U. Nockel, A. D. Stone, J. Faist, D. L. Sivco, A. Y. Cho, *Science* **280**, 1556 (1998).

- [15] A. F. J. Levi, R. E. Slusher, S. L. McCall, J. L. Glass, S. J. Pearton, and R. A. Logan, *Appl. Phys. Lett.* **62**, 561 (1993).
- [16] H. G. L. Schwefel, N. B. Rex, H. E. Tureci, R. K. Chang, A. D. Stone, T. Ben-Messaoud, and J. Zyss, *J. Opt. Soc. Am. B* **21**, 923 (2004).
- [17] J. Wiersig and M. Hentschel, *Phys. Rev. A* **73**, 031802(R) (2006).
- [18] A. Kudrolli, V. Kidambi, and S. Sridhar, *Phys. Rev. Lett.* **75**, 822 (1995).
- [19] X. Yang and C. W. Wong, *Opt. Exp.* **15**, 4763 (2007).
- [20] R. Bose, X. Yang, R. Chatterjee, J. Gao, and C. W. Wong, *Appl. Phys. Lett.* **90**, 111117 (2007). R. Bose, J. Gao, J. F. McMillan, F. W. Sun, X. Yang, C. J. Chen, and C. W. Wong, *Optics Express* **17**, 22474 (2009).
- [21] K.Srinivasan and O.Painter, *Phys. Rev. A* **75**, 023814 (2007).
- [22] D.Englund, D.Fattal, E.Waks, G.Solomon, B.Zhang, T.Nakaoka, Y.Arakawa, Y.Yamamoto and J.Vuckovic, *Phys. Rev. Lett.* **95**, 013904 (2005).
- [23] J.T.Robinson, C.Manolatou, L.Chen and M.Lipson, *Phys. Rev. Lett.* **95**, 143901 (2005).
- [24] Fushman, D. Englund and J. Vuckovic, *Appl Phys Lett* **87** (24) (2005).
- [25] R. Bose, X. D. Yang, R. Chatterjee, J. Gao and C. W. Wong, *Appl Phys Lett* **90** (11) (2007).
- [26] R. Bose, J. F. McMillan, J. Gao and C. W. Wong, *Appl Phys Lett* **95** (13) (2009).
- [27] D. Englund, D. Fattal, E. Waks, G. Solomon, B. Zhang, T. Nakaoka, Y. Arakawa, Y. Yamamoto and J. Vuckovic, *Phys Rev Lett* **95** (1) (2005).
- [28] Y. Ota, M. Shirane, M. Nomura, N. Kumagai, S. Ishida, S. Iwamoto, S. Yoroazu and Y. Arakawa, *Appl Phys Lett* **94** (3) (2009)
- [29] T. Yoshie, A. Scherer, J. Hendrickson, G. Khitrova, H. M. Gibbs, G. Rupper, C. Ell, O. B. Shchekin and D. G. Deppe, *Nature* **432** (7014), 200-203 (2004).
- [30] J. P. Reithmaier, G. Sek, A. Löffler, C. Hofmann, S. Kuhn, S. Reitzenstein, L. V. Keldysh, V. D. Kulakovskii, T. L. Reinecke and A. Forchel, *Nature* **432** (7014), 197-200 (2004).

- [31] E. Peter, P. Senellart, D. Martrou, A. Lemaitre, J. Hours, J. M. Gerard and J. Bloch, *Phys Rev Lett* **95** (6) (2005).
- [32] P. Michler, A. Kiraz, C. Becher, W. V. Schoenfeld, P. M. Petroff, L. D. Zhang, E. Hu and A. Imamoglu, *Science* 290 (5500), 2282-+ (2000).
- [33] A. Imamoglu, K. Hennessy, A. Badolato, M. Winger, D. Gerace, M. Atature, S. Gulde, S. Falt and E. L. Hu, *Nature* 445 (7130), 896-899 (2007).
- [34] D. Englund, A. Faraon, I. Fushman, N. Stoltz, P. Petroff and J. Vuckovic, *Nature* 450 (7171), 857-861 (2007).
- [35] L. M. Duan and H. J. Kimble, *Phys Rev Lett* 92 (12) (2004).
- [36] E. Waks and J. Vuckovic, *Phys Rev Lett* 96 (15) (2006).
- [37] V.S.C. Manga Rao and S. Hughes, *Phys. Rev. B* 75, 205437 (2007);
- [38] D. E. Chang, A. S. Sorensen, E. A. Demler and M. D. Lukin, *Nat Phys* 3 (11), 807-812 (2007).
- [39] V. S. C. M. Rao and S. Hughes, *Phys Rev Lett* 99 (19) (2007).
- [40] J. Gao, F. W. Sun and C. W. Wong, *Appl Phys Lett* 93 (15) (2008).
- [41] E. Viasnoff-Schwoob, C. Weisbuch, H. Benisty, S. Olivier, S. Varoutsis, I. Robert-Philip, R. Houdre and C.J.M. Smith, *Phys. Rev. Lett.* 95, 183901 (2005).
- [42] E. Waks and J. Vuckovic, *Phys. Rev. Lett.* **96**, 153601 (2006).
- [43] S. Mookherjea, J. S. Park, S. H. Yang and P. R. Bandaru, *Nat Photonics* 2 (2), 90-93 (2008).
- [44] J. Topolancik, B. Ilic and F. Vollmer, *Phys Rev Lett* 99 (25), 253901 (2007).
- [45] L. Sapienza, H. Thyrrstrup, S. Stobbe, P. D. Garcia, S. Smolka and P. Lodahl, *Science* 327 (5971), 1352-1355 (2010).

Chapter 2

Interior whispering gallery modes in asymmetric resonate cavities with directional emission

2.1 Introduction to asymmetric resonant cavities

Photon confinement and processes in microcavities [1-3] are critical for a vast span of fundamental studies and applications, ranging from ultra-low threshold microcavity lasers; nonlinear frequency generation [4-5]; dynamic filters and memory for communications; to interactions of atoms with cavity modes in both strong and weak coupling regimes in cavity quantum electrodynamics (QED) [6-7]. Characterized by the cavity quality factor (Q ; photon lifetime) and modal volume (V ; field intensity per photon), 2-dimensional (2D) disk-like resonant structures have achieved remarkable Q up to $\sim 10^8$ with $V \sim 450(\lambda/n)^3$ [2]. A desirable characteristic of these planar whispering gallery mode resonators is that of directional emission, without significant Q -spoiling from the loss of rotational symmetry [8-11]. Different approaches have been explored to show directional lasing from certain special cavity modes in far field distribution by deforming semiconductor or polymer circular microcavities into quadrupole shape[8], stadium [12], spiral shape and line defect [13] with a critical and optimized deformation parameter. These asymmetric resonant cavities (ARC) also have potential applications in the study of disorder and localization in mesoscopic systems as well as, quantum chaos [14] in the diffusive limit. In this Chapter, we show our unique approach to design ARC with interior whispering gallery modes and characterize their directional radiation in monolithic silicon microcavities using angle-resolved tapered fiber coupling techniques and near-infrared images.

2.2 Design of ARCs with interior whispering gallery modes

The ARC we construct here possess whispering gallery modes spatially located deep inside the resonator [15]. These cavities have the special property that one can inscribe into the boundary a one-parametric family of p -periodic orbits of the associated billiard-map. The shapes of such resonators are constructed numerically as a solution of a nonholonomic dynamical system [15]. Here we demonstrate a class of resonators with a family of 4-periodic orbits. The involute of all these 4-periodic orbits forms the rational caustic of the shape. In the surface of section (SOS) plot which represents the classical ray motion in phase space [16], a rational caustic corresponds to an invariant curve consisting of periodic orbits. Under slight perturbation this curve breaks up and a near integrable region appears with the usual periodic orbits surrounded in phase space by elliptic islands, invariant curves and chaotic regions. This region can be seen in the SOS of Figure 2.1(a) which is called the interior whispering gallery (IWG) region. One would expect a family of quasimodes or resonances localized near the original rational caustic. Light will mainly escape at the location where the near integrable region resulting from the rational caustic is closest to the line of total internal reflection. Emission is expected to have strong directionality where half of the total radiation comes from positions according to $\phi = 90^\circ$, $\theta \sim 45^\circ$ or 135° in SOS map with lateral divergence angle of $\sim 11^\circ$ in the azimuthal direction.

Analogous to whispering gallery modes (WGM) which are shown in Figure 2.1(c) and has $Q \approx 3.0 \times 10^8$, one can also find a family of IWG modes which are

supported near the rational caustic and has $Q \approx 1.8 \times 10^4$ as shown in Figure 2.1(b). We calculate TM modes and Q factors by reducing the three-dimensional Maxwell equations to a 2D resonance problem and solve this with a boundary integral method [17]. The size and geometry of the ARC in the simulations are the same with the fabricated ARC. Our analysis also shows that these IWG modes have linear modal volumes $\sim 10 (\lambda/n)^3$ and nonlinear modal volumes $\sim 50 (\lambda/n)^3$ [5]. In order to study the intrinsic loss mechanisms in the ARC, slight perturbations to the cavity shape are introduced to investigate numerically the effects of sidewall disorder roughness (in the actual fabrication) on Q s for both the fundamental WGMs and IWG modes. The intrinsic loss mechanisms in microcavities include radiation loss, scattering loss, material absorption and surface absorption [18]. For microdisks with current modal volumes, surface and material absorption-limited Q s are typically on the order of 10^6 [18]. Because experiments of the fabricated ARC show that total Q s are on the order of 10^3 , surface and material absorption losses are negligible here. For WGMs, the radiation Q is theoretically $\sim 10^8$ so that surface scattering will predominantly dominate the total loss. However, for IWG modes, the radiation Q is around 10^4 due to the intentionally constructed asymmetric shape for directional emission so that radiation is the major loss mechanism for ARC with small edge roughness. When the roughness is large enough, scattering loss will turn out to be comparable to radiation loss. Figure 2.1(d) shows an exponential drop of Q for the WGM with increased edge roughness, whereas Q for the IWG is only slightly affected by a perturbation larger than 15 nm. Even when the roughness is larger than 20nm, we still get a less

significant spoiling of Q by boundary imperfection for IWG modes than for WGMs because IWG modes are mostly concentrated along the rational caustic and away from the boundary.

2.3 Nanofabrication of silicon ARCs

Having designed this special class of ARC, we fabricate the resonators from silicon-on-insulator (SOI) wafers consisting of a 200 nm thick Si layer on top of a 3 μm SiO_2 cladding layer. The fabrication process starts with spin-coating of 200 nm thick 495K A6 PMMA (polymethylmethacrylate) on top of the SOI wafer. The designed pattern is written on the PMMA by electron-beam lithography. The exposed PMMA is developed in a solution of MIBK: IPA=1:3 for 55 seconds. A 30 nm chrome mask is deposited on the top of SOI wafer by thermal evaporation. Then an inductively coupled-plasma (ICP) reactive-ion etch with $\text{SF}_6:\text{C}_4\text{F}_8$ gas chemistry transfers the mask into the top Si layer. After the chrome mask is removed, the SiO_2 layer is selective etched in buffered hydrofluoric acid to create the suspended microdisk-like structures [19]. An example scanning electron micrograph (SEM) of a microfabricated resonator is illustrated in Figure 2.2(b), with an estimated line-edge roughness of 17 nm.

2.4 Experimental demonstration of IWG modes with directional emission

2.4.1 Angled-resolved tapered fiber transmission measurement

To characterize the silicon ARC, a tapered optical fiber setup such as described in Ref. [20-21] is used. By keeping an adiabatic taper profile, a SMF-28 fiber is pulled into a tapered fiber with $\sim 1.1 \mu\text{m}$ waist diameter and negligible loss. The tapered fiber is then curved to provide coupling and contact with the edge of the ARC [20]. The radius of curvature of the curved tapered fiber is $\sim 150\mu\text{m}$. Light from an amplified spontaneous emissions (ASE) source, passing through an in-line fiber polarizer and a polarization controller, is evanescently coupled into cavity through tapered fiber. The imaging system consists of a 50x long working distance objective lens and an 8X telescope as shown in Figure 2.2. Figure 2.3(a) shows the taper transmission spectra at different coupling position [(1)-(4)] [as defined in Figure 2.3(b)] for TM-like modes. Different coupling depths at each position reflect the asymmetric property of this resonator. Positions (3) and (4) show better coupling efficiency due to the strongest mode overlap in the evanescent field with the curved tapered fiber. At positions (1) and (2), the coupling to the resonant modes does not show strongly and asymmetric Fano lineshapes [22] also appear which we suspect are due to an interference pathway between a direct background (weak tapered fiber cavity) and indirect resonant (ARC) pathway. Figure 2.3(c) shows transmission for both TE-like and TM-like polarizations at position (3). TM-like mode is selected in measurement due to its stronger coupling and significantly reduced sensitivity to cavity edge roughness [19].

We perform our tapered fiber coupling measurements along different coupling angles to study the radiation directionality. The transmission spectra in Figure 2.4(a)

show that two distinct mode families with free spectral range ~ 11 nm are strongly supported in this ARC. To identify these families, we examined the coupling depth versus θ [the coupling angle between the resonator and the fiber as defined in Figure 2.3(b)] at position (3). In Figure 2.4(b), there exists a critical angle $\theta \sim 30^\circ$ for the IWG modes where best coupling occurs. For the WGMs, no peaks appear and the coupling depth decreases continuously, which shows that the mode overlap between the WGMs and fiber mode decreases when the tapered fiber is far away from the tangent position. This gives a clear indication that we can distinguish IWG modes and WGMs from different coupling-angle dependences. The strongest coupling strength tells us the cavity mode radiation is strongest in this direction, which matches consistently with our numerical predictions of directional emission. We also perform control measurements of WGMs in circular microdisk as a comparison. The coupling depth decreases exponentially as we expect, and the slight discrepancy between the WGMs in our ARC and WGMs in circular microdisk is due to the asymmetric shape of our resonator. Inset of Figure 2.4(b) shows calculated mode overlaps, which are proportional to the coupling depths, between cavity modes and the fiber mode. We observe consistently the strongest mode overlap between the IWG modes and the fiber mode at $\theta \sim 45^\circ$, which matches our experimental result. We attribute the off-set between the measured and calculated peak positions primarily to the small deviation between our design and the actual shape, and uncertainties in the exact angular determination.

To characterize the quality factor of IWG modes, feedback-controlled piezoelectric stages are used to control the lateral taper-cavity separation g , which is illustrated in the inset of Figure 2.5(b). The transmission spectrum in Figure 2.5(a) shows a loaded Q of 2800 for IWG mode at 1543.44 nm when $g = 0$. Note that the WGM typically shows a larger Q of 8000 than IWG mode due to the increased leakage of IWG modes from directional emission. In Figure 2.5(b), the loading effect diminishes as g increases and the estimated intrinsic cavity Q is ~ 6000 for IWG mode. The measured Q deviates from the numerical predictions due to increased surface scattering in the vertical direction (not captured in simulations).

2.4.2 Near-infrared imaging of modes radiation

To investigate individual mode distribution in ARC, Figure 2.4(c) shows the near-infrared images using a tunable laser and a ThermCAM Merlin near-infrared camera. When the wavelength is tuned on-resonance with the IWG mode, as shown in Figure 2.4(c2), only three bright scattering regions which represent the directional emission of the ARC are observed. This corresponds directly to three regions of high intensity in the IWG mode shown in Figure 2.1(b), and also agrees with three peaks within the IWG region in the SOS map in Figure 2.1(a). For comparison figure 2.4(c1) shows WGM mode when tuned on-resonance, and scattering from the entire boundary can be observed. This confirms our simulation result that scattering loss of WGM modes due to edge roughness is dominated while IWG modes is not sensitive as WGM to Rayleigh scattering from edge roughness. As a reference, a near-infrared image with

off-resonance condition is also illustrated in Figure 2.4(c3) where only the fiber mode is observable.

2.5 Conclusion

In summary, we have constructed numerical methods to design remarkable asymmetric resonant cavities with high Q interior whispering gallery modes and observed experimentally the radiation directionality of these modes with Q value of ~ 6000 through angle-resolved tapered fiber coupling techniques. The Q values of these modes are not spoiled by slight edge boundary imperfection, which is an advantage for application and proves the usefulness of resonators with rational caustics together with the directionality. Our design and characterization of interior whispering gallery modes in silicon asymmetric resonant cavities open the door to engineer the asymmetric cavity shape and achieve its application in microcavity-based QED and lasing with directional emission in the future.

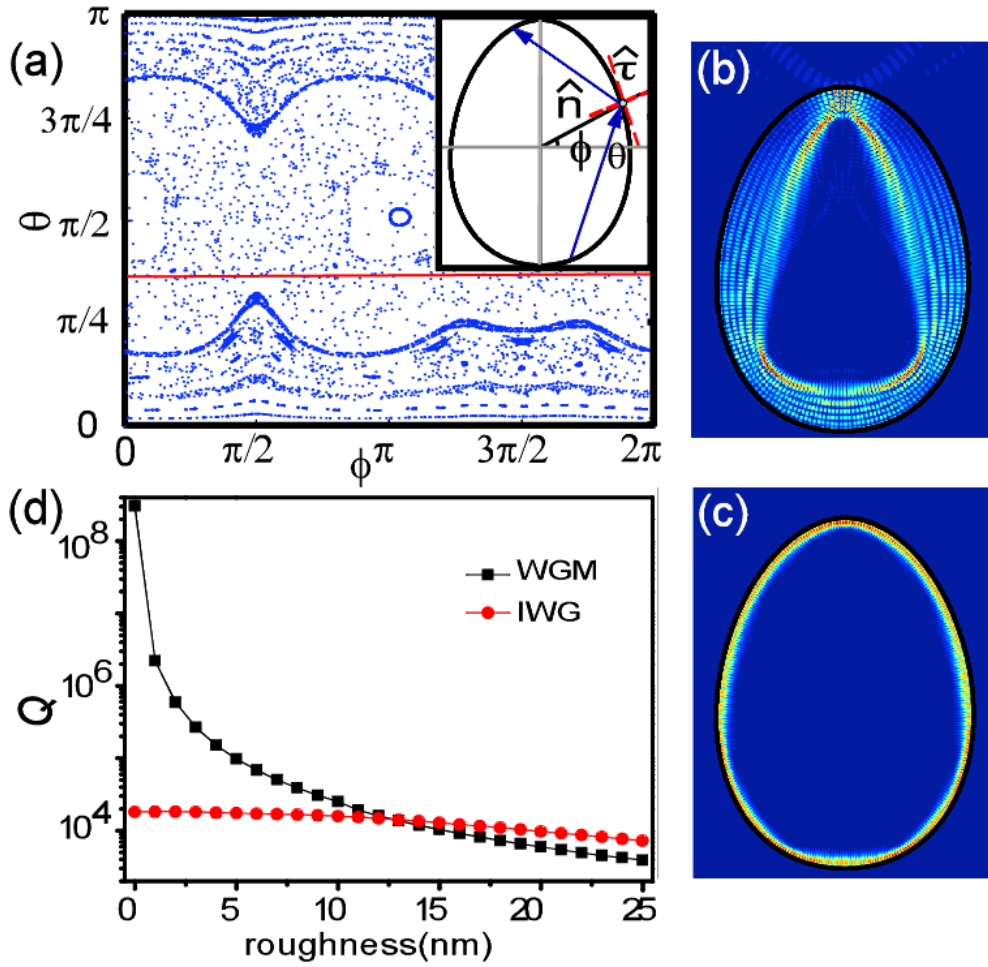


Figure 2.1 (a) Poincaré surface of section plot. Horizontal axis ϕ represents the intercept point of the ray and the cavity boundary, and vertical axis θ represents the incident angle between the ray and the tangent line of the boundary. The red solid line corresponds to the total internal reflection. (b) IWG mode supported near the rational caustic and (c) the fundamental WGM mode. (d) Numerical simulations of Q s for WGMs (squares) and IWG modes (circles) versus cavity edge roughness.

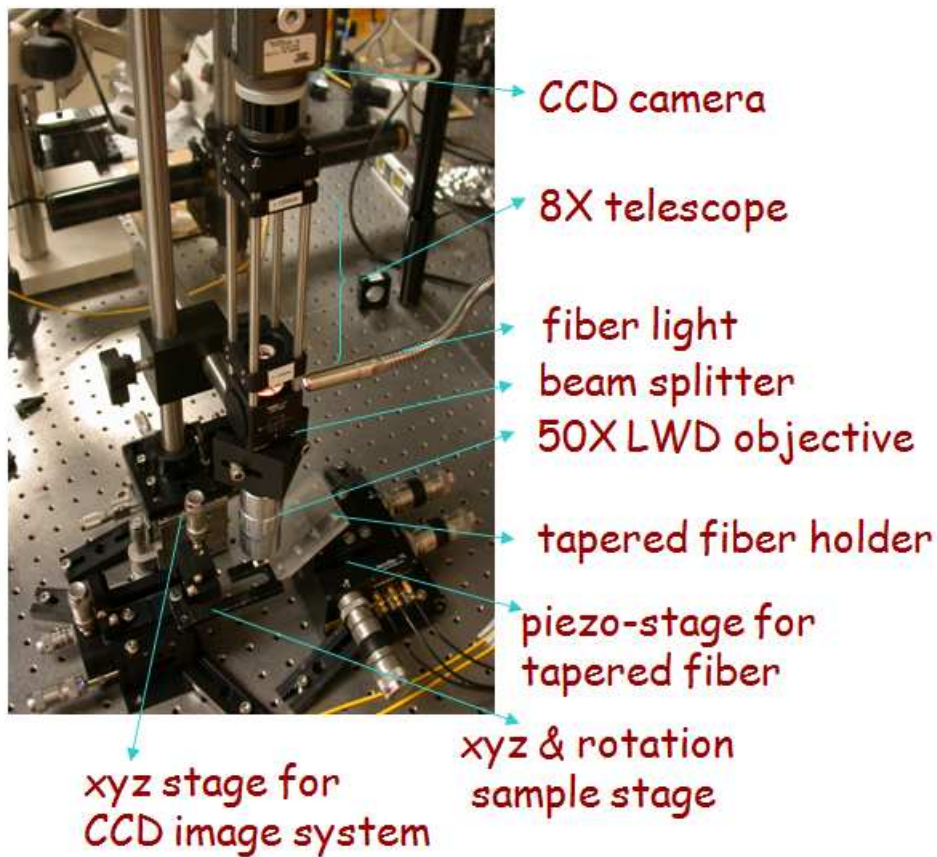


Figure 2.2 Experimental setup of tapered fiber characterization measurement. Light from ASE source, passing through an in-line fiber polarizer and a polarization controller, is evanescently coupled into cavity through tapered fiber. Fiber transmissions are monitored on optical spectrum analyzer to observe cavity resonances, and vertical radiations from the top of ARCs are captured by near-infrared camera.

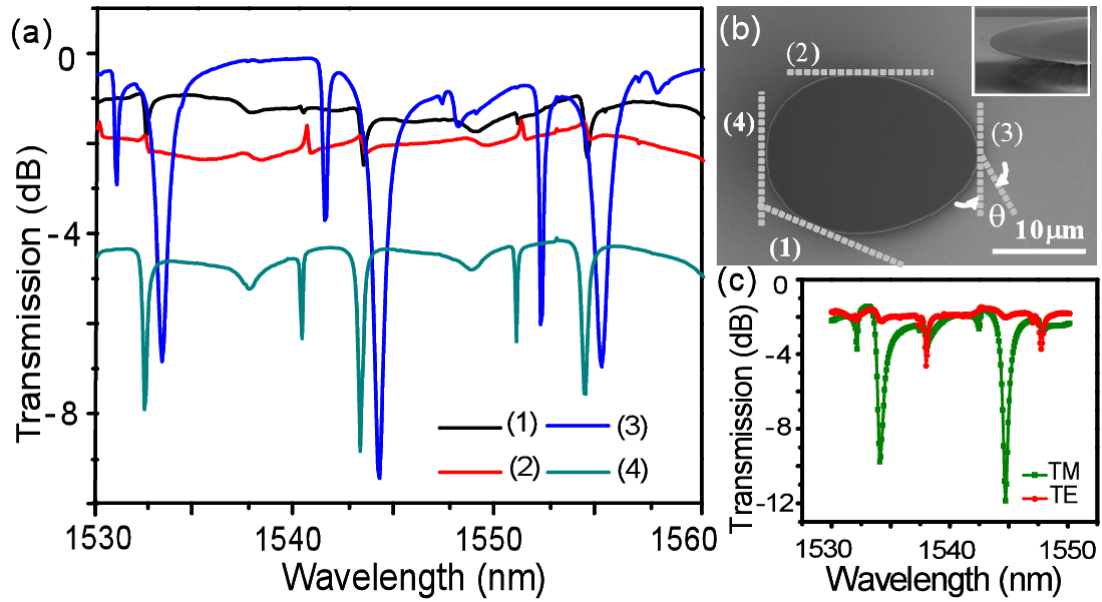


Figure 2.3 (a) Normalized transmission spectra when the taper touches the resonator side in tangential direction at different positions. (b) SEM of fabricated suspended silicon ARC on oxide pedestal. Dotted lines (--) show tapered fiber spatial probe positions [(1) - (4)]. (c) Transmission spectrum for TE-like and TM-like polarization.

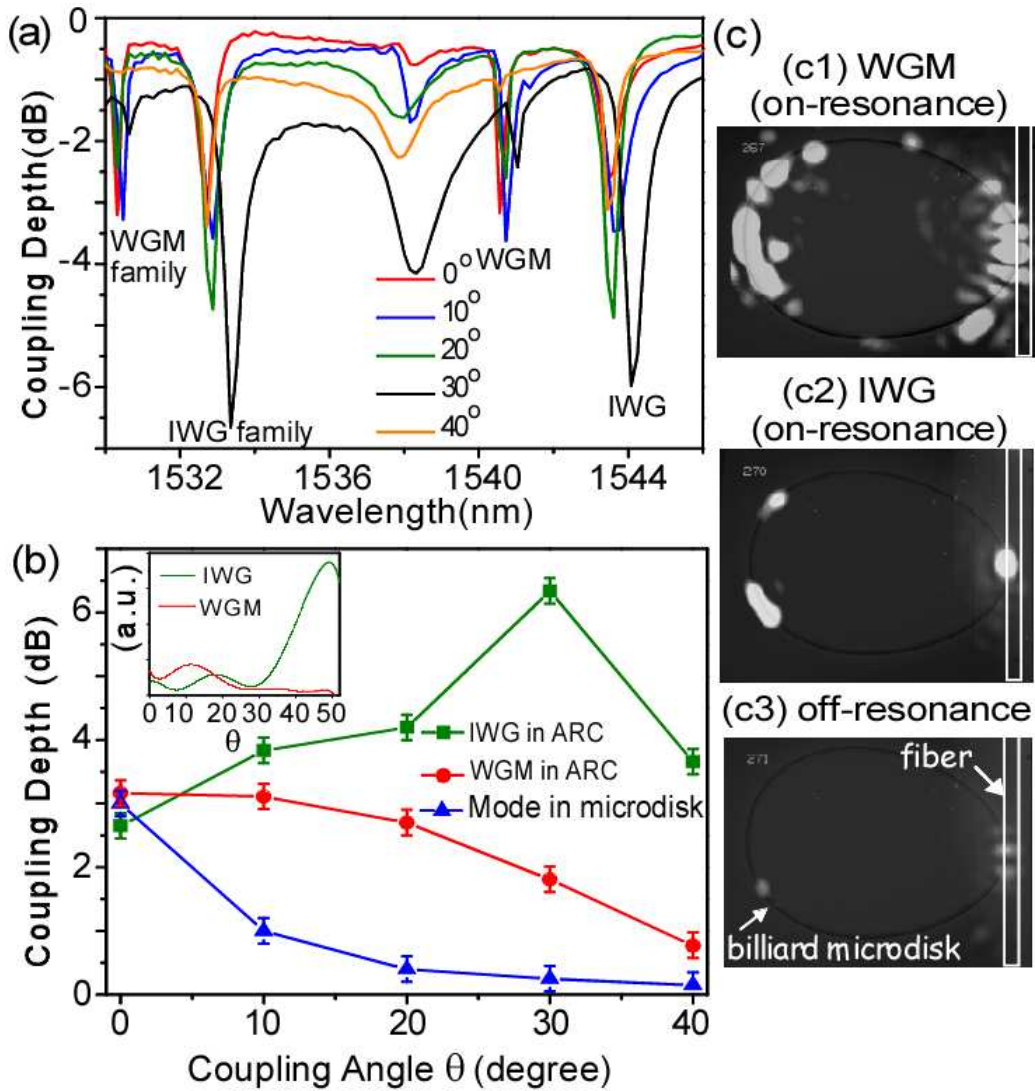


Figure 2.4 (a) Normalized transmission spectra when the taper is positioned along different coupling angle θ at position (3). (b) Experimental and numerical (inset) results for coupling depth versus θ . (c) Near-infrared images of IWG modes (c2) and WGMs (c1).

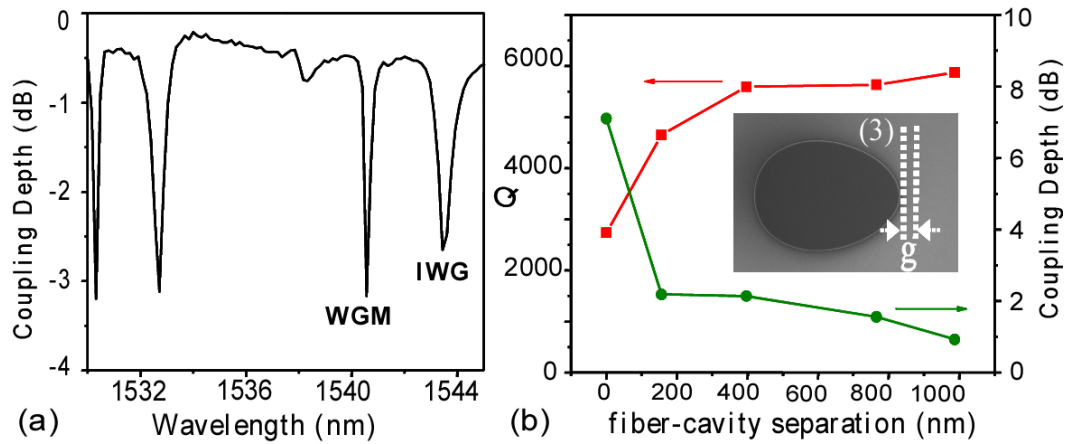


Figure 2.5 (a) Transmission spectrum when fiber-cavity separation $g = 0$. (b) Coupling depth (circles) and Q factor (squares) as functions of g . Inset: Experiment illustration for measuring the Q value.

Bibliography

- [1] R. K. Chang and A. J. Campillo (editors), *Optical Processes in Microcavities* (Advanced Series in Applied Physics; vol. **3**), World Scientific Publishers, Singapore, 1996.
- [2] K. J. Vahala (editor), *Optical Microcavities* (Advanced Series in Applied Physics; vol. **5**), World Scientific Publishers, Singapore, 2005 ; K. J. Vahala, *Nature* **424**, 839 (2003).
- [3] S. Noda, M. Fujita, and T. Asano, *Nature Photonics* **1**, 449 (2007).
- [4] T. Carmon and K. Vahala, *Nature Physics* **3**, 430 (2007).
- [5] X. Yang and C. W. Wong, *Optics Express* **15**, 4763 (2007).
- [6] T. Aoki, B. Dayan, E. Wilcut, W. P. Bowen, A. S. Parkins, T. J. Kippenberg, K. J. Vahala and J. Kimble, *Nature* **443**, 671 (2006).
- [7] R. Bose, X. Yang, R. Chatterjee, J. Gao, and C. W. Wong, *Appl. Phys. Lett.* **90**, 11117 (2006).
- [8] C. Gmachl, F. Capasso, E. E. Narimanov, J. U. Nockel, A. D. Stone, J. Faist, D. L. Sivco, A. Y. Cho, *Science* **280**, 1556 (1998).
- [9] A. F. J. Levi, R. E. Slusher, S. L. McCall, J. L. Glass, S. J. Pearton, and R. A. Logan, *Appl. Phys. Lett.* **62**, 561 (1993).
- [10] H. G. L. Schwefel, N. B. Rex, H. E. Tureci, R. K. Chang, A. D. Stone, T. Ben-Messaoud, and J. Zyss, *J. Opt. Soc. Am. B* **21**, 923 (2004).
- [11] J. Wiersig and M. Hentschel, *Phys. Rev. A* **73**, 031802(R) (2006).
- [12] W. Fang, H. Cao and G.S. Solomon, *Appl. Phys. Lett.* **90**, 081108 (2007).
- [13] A. Tulek and Z.V. Vardeny, *Appl. Phys. Lett.* **90**, 161106 (2007).
- [14] A. Kudrolli, V. Kidambi, and S. Sridhar, *Phys. Rev. Lett.* **75**, 822 (1995).
- [15] Y. Baryshnikov, P. Heider, W. Parz, and V. Zharnitsky, *Phys. Rev. Lett.* **93**, 133902 (2004).

- [16] L. Reichl, *The transition to chaos in conservative classical systems: Quantum Manifestations*, Springer-Verlag, New York, 1992.
- [17] Jan Wiersig, *J. Opt. A: Pure Appl. Opt.* **5**, 53 (2003).
- [18] M. Borselli, T. J. Johnson and O. J. Painter, *Optical Express* **13**, 1515 (2005).
- [19] M. Borselli, K. Srinivasan, P. E. Barclay, and O. J. Painter, *Appl. Phys. Lett.* **85**, 3693 (2005).
- [20] I.-K. Hwang, S.-K. Kim, J.-K. Yang, S.-H. Kim, S. H. Lee, and Y.-H. Lee, *Appl. Phys. Lett.* **87**, 131107 (2005).
- [21] K. Srinivasan, P.E. Barclay, M. Borselli, and O. Painter, *IEEE Journal on Selected Areas in Communications* (special issue on photonic crystals), Vol. **23**, No. 7, pp. 1321-1329, July 2005.
- [22] X. Yang, C. Husko, C. W. Wong, M. Yu, and D.-L. Kwong, *Appl. Phys. Lett.* **91**,051113 (2007).

Chapter 3

Air-slot mode-gap confined photonic crystal slab cavities with ultras-small effective mode volume

3.1 Introduction

Many optical cavities with Q and small V have been developed and fabricated, including Fabry-Perot cavities [1], microspheres [2], silicon and silica whispering gallery type resonators [3-4] and photonic crystal nanocavities [5-6]. In particular, the 2D photonic crystal cavity with a single emitter possesses remarkable possibilities towards efficient single photon sources or strong coupling regime for quantum communications and computing. Silicon photonic crystal cavities have achieved remarkable Q up to $\sim 10^6$ experimentally but with mode volume traditionally limited to sizes that are on the order of the wavelength of light. From the definition of the

normalized dimensionless effective mode volume $V_{eff} = \frac{\int \epsilon(\vec{r}) |\vec{E}(\vec{r})|^2 d^3r}{\epsilon(\vec{r}_{max}) \max[|\vec{E}(\vec{r})|^2]} \left(\frac{2n(\vec{r}_{max})}{\lambda} \right)^3$

(where \vec{r}_{max} is the location of the maximum squared electric field), we know that mode volume can be reduced by increasing the mode maximum electric field and localizing the mode maximum in the low index region. Reducing V_{eff} in cavities enables one to control the degree of light-matter interaction for processes such as nonlinear optics [7] and cavity QED [8]. The Purcell factor for an emitter in a resonant cavity is inversely proportional to V_{eff} [9], and the Rabi frequency is inversely proportional to the square root of V_{eff} [10]. Towards this objective, Robinson *et al.* [11] have proposed one-dimensional microcavities with ultrasmall mode volume by using dielectric discontinuities to enhance local field. In this Chapter, we introduce an air slot to the point-defect nanocavity (L3 cavity with three holes missing in the triangle

lattice) in a 2D photonic crystal slab and characterize it through tapered fiber coupling. However quality factors of air-slot L3 or 1D photonic crystal cavities are typically not very high because the structures suffer large vertical radiation loss at the abrupt termination of the air-slot. We further examine mode-gap confined nanocavities in a 2D photonic crystal slab with a non-terminated air-slot, which have both high Q and ultrasmall mode volume for the study of light matter interactions.

3.2 Design and characterization of air-slot L3 cavity

Silicon L3 cavity supports a localized mode as shown in Figure 3.1 (a), with Q factor of 10^5 and mode volume V of $0.7(\lambda/n)^3$ [12]. The mode has the maximum squared electric field located in the center of the silicon defect region, and $|\vec{E}(\vec{r})|^2$ along x -direction is shown as the black curve in Figure 3.1(c). When we introduce an infinitesimal air slot, the normal component of the electric displacement is continuous across the boundary of the air slot walls, thus $\epsilon_0 E_{air} = \epsilon_{si} E_{si}$. Compared with L3 cavities, in slot cavity $\max |\vec{E}(\vec{r})|^2$ can be theoretically increased by $\epsilon_{si} / \epsilon_0 = n_{si}^2$. Together with $n(\vec{r}_{\max})=1$, a total decrease is $n_{si}^5 \sim 510$ times for the dimensionless effective mode volume.

The air slot plays an important role for the realization of strong field localization, however the decrease fold of V_{eff} is usually smaller compared to the theoretical value for the infinitesimal air slot because of the minimum slot width we can practically get in the fabrication. We perform three-dimensional finite-difference

time-domain (FDTD) simulations to numerically evaluate the properties of the proposed cavity. For the ab initio calculations, we set a lattice constant $a=420\text{nm}$, an air-hole radius $r=122\text{nm}$, a slab thickness $t=250\text{nm}$, a slab refractive index $n_{si}=3.48$ and hole shifts $s_1=0.2a$, $s_2=0.025a$, $s_3=0.2a$. For slot width $s=40\text{nm}$ (grid spacing is set to be 13nm), Figure 3.1(b) shows the mid-slab electric field of the fundamental mode, and red curve in Figure 3.1(c) explicitly shows the enhanced electric field because of the slot confinement. The calculated Q is ~ 2000 and mode volume is $0.005(\lambda/n)^3$ which is much smaller than other reported cavity designs [13].

An example SEM of the fabricated silicon suspended photonic crystal slot cavity is illustrated in Figure 3.2(a). The fabricated devices with s_1 tuning have hole radius 10% larger than the designed parameters and slot width $s=100\text{nm}$. We do post-simulations according to the fabricated dimensions, and the resonant mode and band structure are shown in Figure 3.2(b) (c). The localized mode has $Q\sim 10^3$ at normalized frequency $f = 0.34(a/\lambda)$ with mode volume of $0.02(\lambda/n)^3$. Mode volume is larger than the designed value because of the 100nm slot width. Similar tapered fiber in Chapter 2 is used to characterize the fabricated cavity. Position and direction are precisely controlled to bring the tapered fiber to contact with the cavity surface (see Figure 3.3(a)), and resonance features appear in the transmission spectra in Figure 3.3(b). For different devices, we do see the cavity resonances shift to shorter wavelength for devices with larger air hole radius. These resonances are sensitive to the fiber position and the polarization of the input light. Figure 3.3(c) clearly shows the distinguishable transmission spectra under TE-polarized and TM-polarized input light. In the

experiment piezoelectric stages are used to control the vertical tapered fiber-cavity separation Δz . Figure 3.4(left) shows the transmission spectra as a function of fiber-cavity gap. The loading effects diminish as the taper is positioned further and further above the cavity, until a regime is reached where the resonant frequency and linewidth do not change. For the particular device shown in Figure 3.2(a) when $\Delta z = 0$, the resonance wavelength is around 1268nm and an initial Q estimate of 26. This is a higher bound for resonance wavelength and lower bound for cavity Q due to the taper's loading effects. When Δz gets larger to be several hundred nanometers away from the surface, the resonance wavelength is approaching 1256nm (which matches the resonant frequency in the simulation) and linewidth is getting narrower as shown in Figure 3.4(right). From coupled mode theory, the intrinsic Q can be expressed as follows [12]: $Q_{intrinsic} = Q_{measure} / \sqrt{T}$. The transmittance T is defined as the ratio of the transmitting energy in the presence of the cavity near the coupling fiber to the energy in the absence of the cavity. From the large contrast of the red curve in Figure 3.4(left), the intrinsic Q is estimated to be around 100. A deviation from the numerical predictions is mainly due to roughness scattering from imperfect fabrication currently.

3.3 Design of air-slot PhC cavities with high Q and

ultrashall V_{eff}

Furthermore, we experimentally study air-slot mode-gap photonic crystal cavities based on the original proposal in Ref. [14]. A non-terminated air-slot is added to

width-modulated line-defect photonic crystal cavities (shifting air holes away from waveguide [15]) to create ultrasmall mode volume cavities. However, other work on high Q heterostructure air-slot cavities [16] emphasize the positive dispersion of slotted photonic crystal waveguide (PhCWG) mode and form the cavities by locally compressing the lattice to pull the eigenstate up in the band gap, opposite to conventional mode-gap cavities [15,17]. To better understand the modes, we first investigate the modes and dispersion in slotted PhCWG. We perform three-dimensional band structure calculation for slotted W1 waveguide in Figure 3.5(a). Three modes are shown in Figure 3.5(b-I, II, III). Compared with the field distribution of standard W1 PhCWG, Mode I and II can be respectively traced back to W1 waveguide fundamental even mode and high order odd mode inside the band gap [18, 19]. The electric field of mode I inside the air slot region is the E_y component and the existence of air slot enhances this component because the electric displacement in y direction needs to be continuous across the slot boundary. However the electric field of mode II inside the air slot region is the E_x component and is not affected since its polarization is parallel to the slot. This also explains why mode I appears closer to the air band, and even has higher frequency than mode II. Note that we have mode III in the band gap, which shows a positive slope in the first Brillouin zone. While the mode is similar to the mode discussed in Ref. [20], the origin of this mode is not well explained earlier. By comparing the Hz field of mode III with the index-guided modes in W1 waveguide, we note mode III actually originates from the second index-guided mode shown in Ref. [18] below the projected bulk modes. This mode has E_y

component in the slot, and so the frequency is pulled up to be within the photonic band gap.

When we generate cavities by locally shifting the air holes away from the center of waveguide, a mode-gap region is formed and cavity modes are created just below the slotted PhCWG transmission band. There are three possible modes (Figure 3.6). Confirmed from the mode frequency and symmetry, mode in Figure 3.6(a) is due to the mode gap of slotted waveguide mode I in Figure 3.5(b-I) and is expected to have both high Q and ultrasmall V_{eff} . This is also the only accessible high Q mode in the experiment through even mode excitation (from strip waveguide). The mode maximum squared electric field is in the air-slot center region [Figure 3.6(a)]. Compared with mode-gap confined cavities without slot, the dimensionless effective mode volume theoretically shows a total decrease of 500 times. Figure 3.6(b) represents the mode with the same odd symmetry as mode II in slotted waveguide, and Figure 3.6(c) represents the low Q mode which couples to PhCWG mode III without mode-gap confinement.

3.4 Experimental setup and characterization for air-slot mode-gap PhC cavities

An example SEM of the electron-beam nanofabricated cavity is illustrated in Figure 3.7(a), with 220 nm thick Si and suspended with a sacrificial wet-etch [21]. 3D FDTD simulations evaluate the fabricated cavity mode properties with $a = 490\text{nm}$, $r = 0.34a$,

$t = 0.449a$, $n_{\text{si}}=3.48$, $d_a=0.0286a$, $d_b=0.019a$ and $d_c=0.0095a$. For slot width $s=80\text{nm}$ (grid spacing at 28nm), the cavity supports a high Q localized even mode (see Figure 3.7(b)) with Q factor of 1.6×10^5 and mode volume V_{eff} of $0.02 (\lambda/n_{\text{air}})^3$. The Q/V_{eff} ratio of $8 \times 10^6 (\lambda/n_{\text{air}})^{-3}$ is much higher than previous reported ultrasmall mode volume cavity designs [11, 13] and the work of air-slot L3 cavity in Section 3.3. Furthermore, the electric field 2D Fourier transform [Figure 3.7(c)] shows small leaky components inside the light cone supporting the high Q character. An in-line PhCWG coupling configuration was utilized to the cavity, with cavity-waveguide distance $L_C=4.5a$ for tunneling [SEM in Figure 3.8(a)]. The base widths of a line defect for a cavity is $\sqrt{3}a$ and the input/output waveguides are $1.05 \times \sqrt{3}a$. Polarization controllers, lensed fibers, and tunable lasers are used for the transverse-electric (TE) polarization launched. Vertical cavity radiation is collected [red region in Figure 3.8(a)] by a $40\times$ objective lens with lock-in amplification to analyze the cavity resonances and Q from the radiation linewidth. Figure 3.8(b-d) illustrate the measured cavity linewidth for different slot widths (80nm and 120nm) and hole radius ($r=0.306a$ and $0.285a$).

For the 80nm slot width devices, Figure 3.8(b) shows a 0.13nm linewidth from Lorentzian fit for a Q of $\sim 12,000$. The measurements are one order of magnitude smaller than the 3D FDTD simulation due to variations of the slot width and roughness of slot edge during fabrication, which degrade the cavity Q . For cavity with smaller hole radius, the band gap and cavity resonance shifts towards longer wavelength [Figure 3.8(b) to 3.8(c)]. When the slot width increases to 120nm, cavity mode shifts close to the air band and becomes very lossy. It is expected that cavity

resonance moves to shorter wavelength and Q factor drops significantly. However, we increase the width of the base waveguide in this case to be $1.2 \times \sqrt{3}a$. This maintains the cavity mode in the middle of the band gap, resulting with measured Q of $\sim 15,000$ [Figure 3.8(d)]. More air-slot cavities with various parameters are examined and quality factors are observed within the range of $12,000 \sim 25,000$.

This experimental demonstration of air-slot mode-gap cavity with both high Q and ultrasmall mode volume provides us a platform to advance cavity QED based on colloidal nanocrystals and silicon nanocavities. Compared to InAs quantum dots, colloidal nanocrystals can be spun on silicon nanocavities as a post-CMOS hybrid integration process. Moreover lead salt nanocrystals can operate at the longer near- to mid-infrared wavelengths. Purcell factor of up to 1500 is possible for air-slot mode-gap confined cavity (with $V_{eff} \sim 0.02$) with quantum dots on the surface of the slot edge (assuming the exciton dipole decay rate is much smaller compared to g, κ under cryogenic temperature), while previous work [8, 22] only show the possibility of 7 to 30 for single-defect photonic crystal nanocavities (such as L3 cavity with $V_{eff} \sim 0.7$ [12]) in the presence of quantum dots induced Q degradation. These illustrate the strong potential of the slot cavity colloidal nanocrystal system to achieve high efficiency single photon source on-demand and even strong exciton-photon coupling in the fiber network communication frequencies.

3.5 Conclusion

In summary, 2D mode-gap air-slot photonic crystal cavities from the negative dispersion waveguide mode have been fabricated and experimentally characterized with Q up to $\sim 10^4$ and mode volume as small as $0.02(\lambda/n_{\text{air}})^3$. Furthermore we discuss the modes existing in the slotted PhCWGs and explain in detail the origins of the air-slot mode-gap confined cavities modes. The air-slot cavity reported here can strongly enhance light-matter interactions, such as the increased Purcell factor and Rabi frequency in fundamental cavity QED studies.

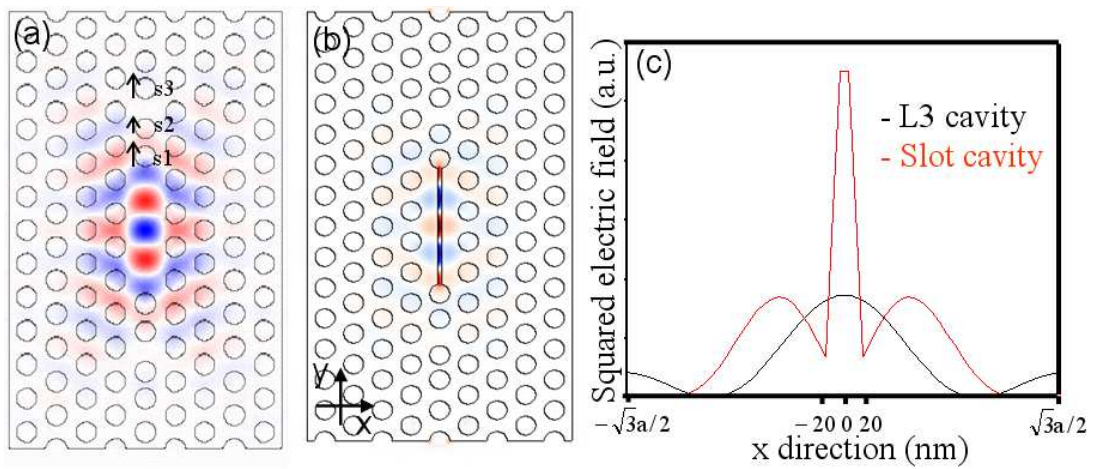


Figure 3.1 (a) E_x field intensity of L3 cavity in the x - y plane. (b) E_x field intensity of air slot cavity in the x - y plane. (c) Squared electric field distribution (black: L3 cavity; red: Slot cavity) along x direction ($y=0$, $z=0$).

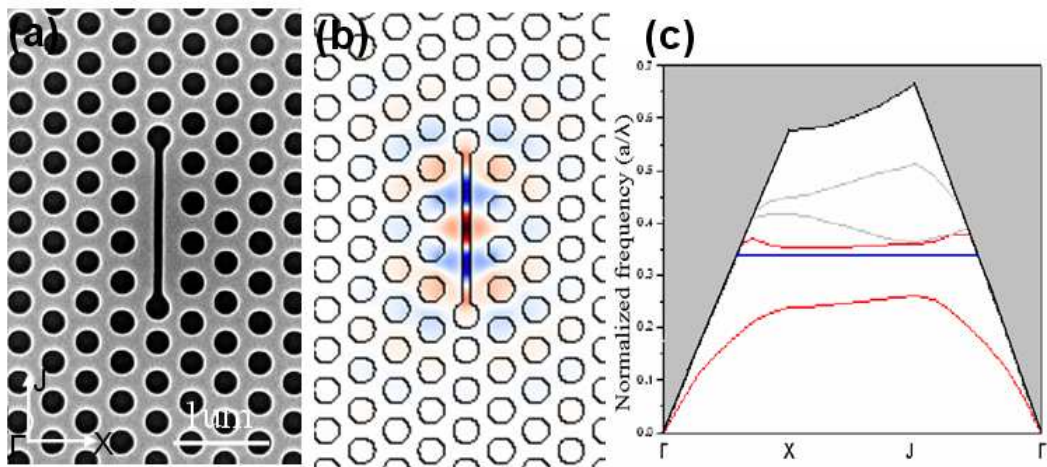


Figure 3.2 (a) SEM of the fabricated cavity with an air slot. Scale bar: 1 μm . (b) E_x field intensity of localized mode calculated from FDTD simulation using the fabricated parameters. (c) TE band structure of silicon air-bridged 2D photonic crystal slab. Blue line indicates the localized mode shown in (b).

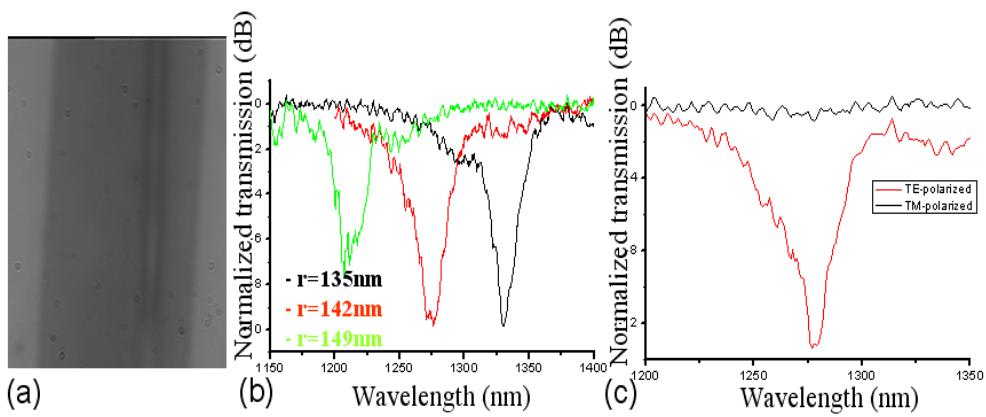


Figure 3.3 (a) Optical micrograph of the tapered fiber aligned along the y axis of the cavity. (b) Normalized taper transmissions for devices with different air hole radius when the taper touches the cavity. (c) Normalized taper transmission when the input light is TE-polarized (red) and TM-polarized (black).

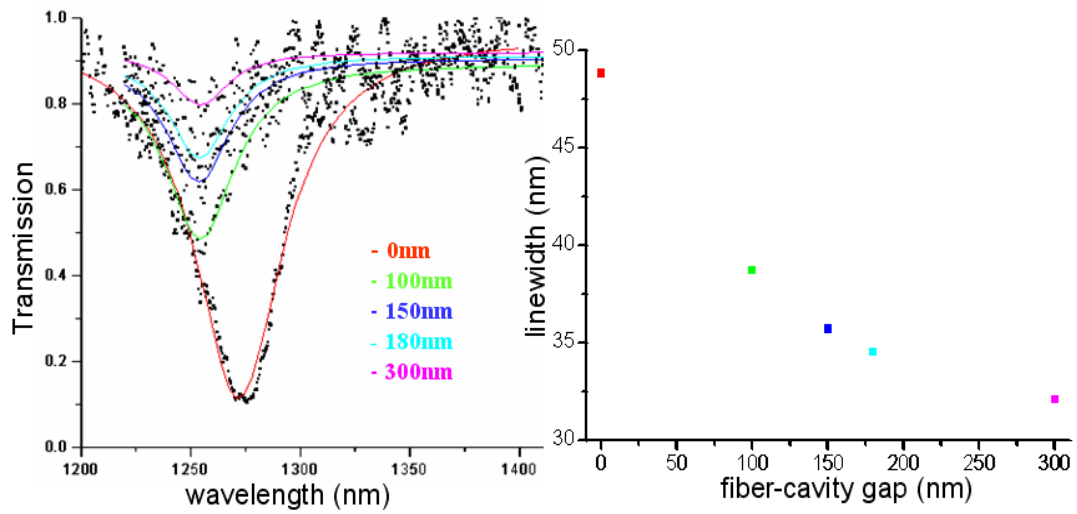


Figure 3.4 (Left) Normalized taper transmissions as a function of fiber-cavity gap. **(Right)** Full widths at the half maximum of the mode as a function of the gap.

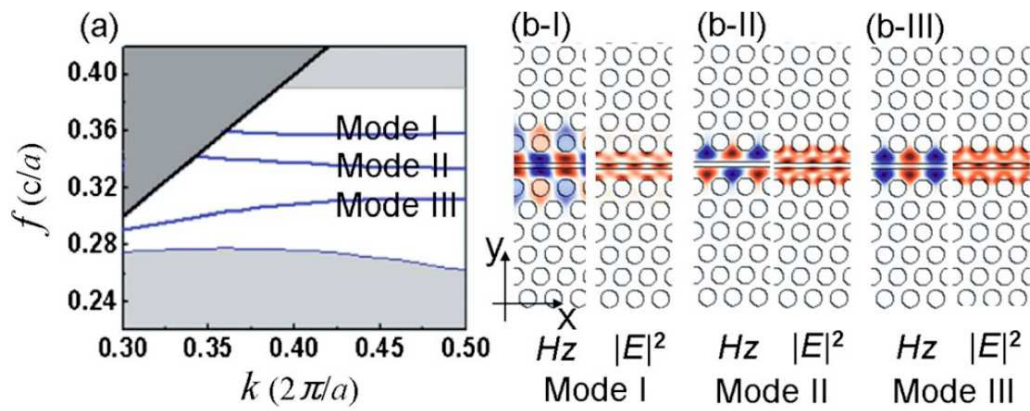


Figure 3.5 (a) Band structure of slotted W1 PhCWG with $a = 490\text{nm}$, $r = 0.34a$, $t = 0.449a$, $n_{\text{Si}}=3.48$ and slot width $s=80\text{nm}$. (b-I, II, III) Field distributions (Left: H_z ; Right: $|E|^2$) of the three modes inside TE band gap.

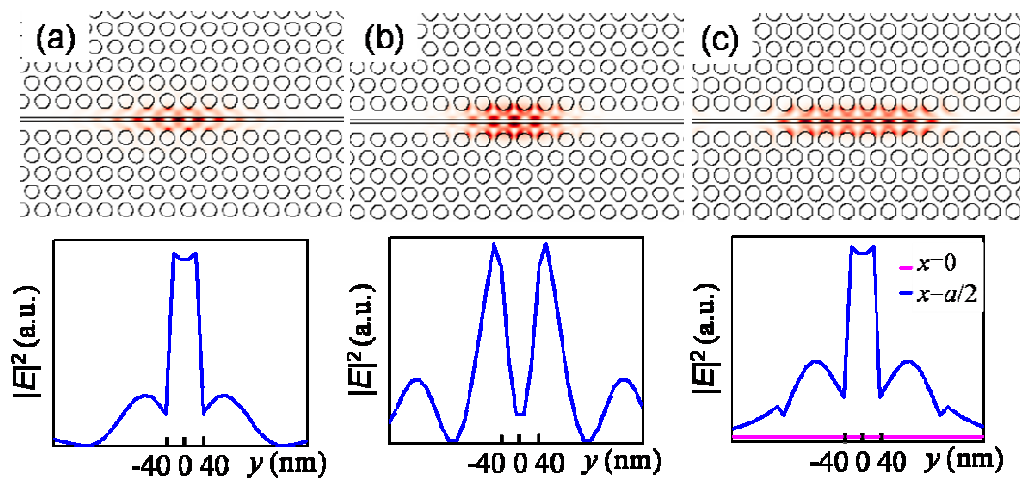


Figure 3.6 (a-c) 2D FDTD simulation of $|E|^2$ spatial distribution and the $|E|^2$ value across the air slot for cavity modes created from photonic waveguide mode I, II, III respectively.

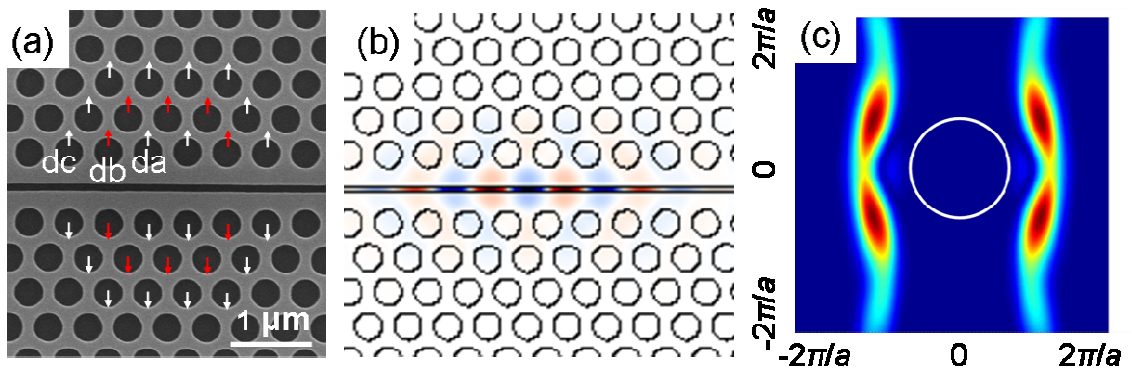


Figure 3.7 (a) SEM of the air-slot mode-gap confined cavity. (b-c) 3D FDTD simulation and Fourier transform of the electric field for cavity mode due to mode-gap effect of waveguide mode I.

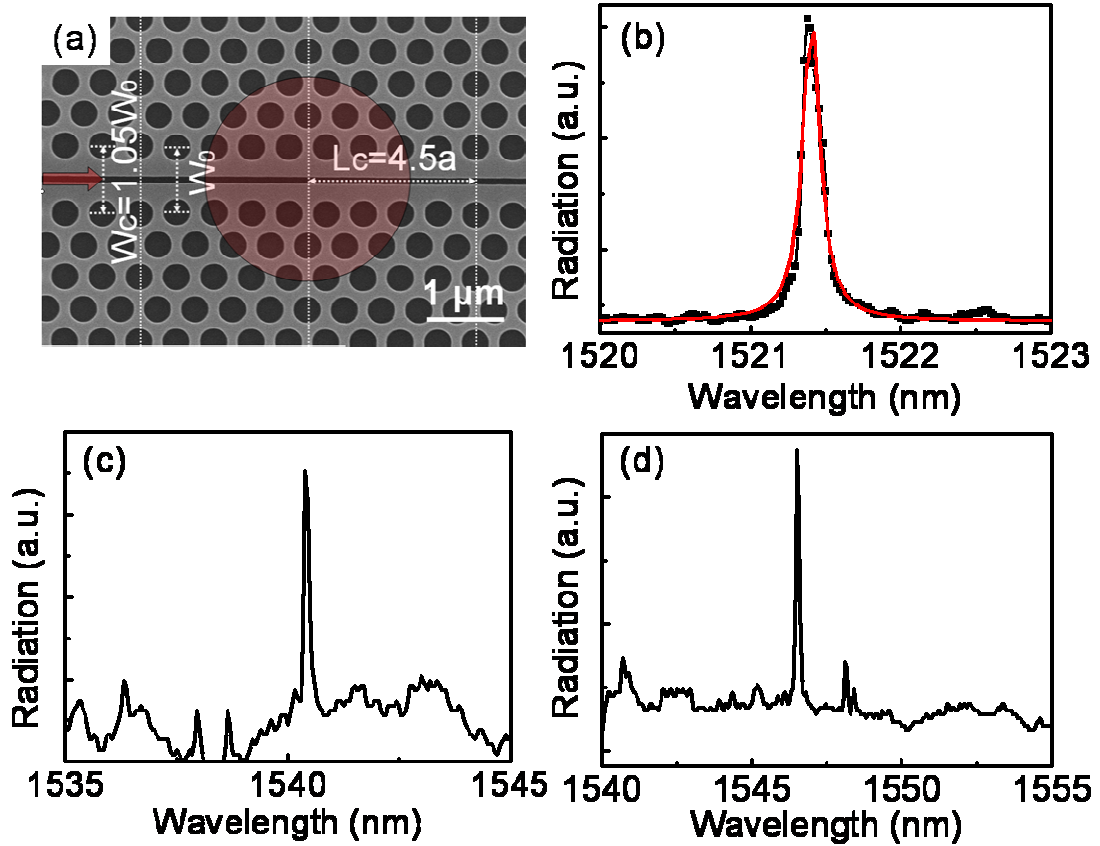


Figure 3.8 (a) SEM of the air-slot mode-gap confined cavity with in-line coupling waveguide. The base width of a line defect $W_0 = \sqrt{3}a$ and the width of input/output waveguides is $W_c = 1.05 \times \sqrt{3}a$. The distance between the cavity and coupling waveguide is $L_c = 4.5a$. Red circle indicates the region from which the radiation signals are collected. (b-d) Radiation spectra of three devices: (b) $W_0 = \sqrt{3}a$, $s = 80\text{nm}$ and $r = 0.306$; (c) $W_0 = \sqrt{3}a$, $s = 80\text{nm}$ and $r = 0.285$; (d) $W_0 = 1.2 \times \sqrt{3}a$, $s = 120\text{nm}$ and $r = 0.285$.

Bibliography

- [1] K. J. Vahala, *Nature* **424**, 839 (2003).
- [2] I. S. Grudinin, A. B. Matsko, and L. Maleki, *Optics Express* **15**, 3390 (2007).
- [3] M. Soltani, S. Yegnanarayanan, and A. Adibi, *Optics Express* **15**, 4694 (2007); S. Xiao, M. H. Khan, H. Shen, and M. Qi, *Optics Express* **15**, 14467 (2007); A. Nitkowski, L. Chen, L., and M. Lipson, *Optics Express* **16**, 11930 (2008); J. Gao, P. Heider, C. J. Chen, X. Yang, C. A. Husko, and C. W. Wong, *Appl. Phys. Lett.* **91**, 181101 (2007).
- [4] D. K. Armani, T. J. Kippenberg, S. M. Spillane and K. J. Vahala, *Nature* **421**, 925 (2003).
- [5] S. Noda, M. Fujita, and T. Asano, *Nature Photonics* **1**, 449 (2007).
- [6] T. Tanabe, M. Notomi, E. Kuramochi, A. Shinya, H. Taniyama, *Nature Photonics* **1**, 49 (2007).
- [7] X. Yang and C. W. Wong, *Opt. Exp.* **15**, 4763 (2007).
- [8] R. Bose, X. Yang, R. Chatterjee, J. Gao, and C. W. Wong, *Appl. Phys. Lett.* **90**, 111117 (2007). R. Bose, J. Gao, J. F. McMillan, F. W. Sun, X. Yang, C. J. Chen, and C. W. Wong, *Optics Express* **17**, 22474 (2009).
- [9] K.Srinivasan and O.Painter, *Phys. Rev. A* **75**, 023814 (2007).
- [10] D.Englund, D.Fattal, E.Waks, G.Solomon, B.Zhang, T.Nakaoka, Y.Arakawa, Y.Yamamoto and J.Vuckovic, *Phys. Rev. Lett.* **95**, 013904 (2005).
- [11] J.T.Robinson, C.Manolatou, L.Chen and M.Lipson, *Phys. Rev. Lett.* **95**, 143901 (2005).
- [12] Y.Akahane, T.Asano, B.S.Song and S.Noda, *Opt. Exp.* **13**, 1202 (2005).
- [13] Z.Zhang and M.Qiu, *Opt. Exp.* **12**, 3988 (2004).
- [14] T.Yamamoto, M.Notomi, H.Taniyama, E.Kuramochi, Y.Yoshikawa, Y.Torii and T.Kuga, *Opt. Exp.* **16**, 13809 (2008).
- [15] E. Kuramochi, M. Notomi, S. Mitsugi, A. Shinya and T. Tanabe, *Appl. Phys. Lett.* **88**, 041112 (2006).

- [16] A. Di Falco, L. O’Faolain and T. F. Krauss, *Appl. Phys. Lett.* **94**, 063503 (2009).
- [17] B. Song, S. Noda, T. Asano and Y. Akahane, *Nature Materials* **4**, 207 (2005).
- [18] C. Jamois, R. B. Wehrspohn, L. C. Andreani, C. Hermann, O. Hess and U. Gösele, *Photonics and Nanostructures: Fundamentals and Applications* **1**,1 (2003).
- [19] J. D. Joannopoulos, S. G. Johnson, J. N. Winn and R. D. Meade, *Photonic Crystals, Molding the Flow of Light*, Second Edition, Princeton, NJ, 2008.
- [20] A. Di Falco, L. O’Faolain and T. F. Krauss, *Appl. Phys. Lett.* **92**, 083501 (2008); J. Wu, C. Peng, Y.-P. Li and Z.-Y. Wang, *Chinese Phys. Lett.* **26**, 014209 (2009).
- [21] S. Assefa, S. J. McNab, and Y. A. Vlasov, *Opt. Lett.* **31**, 745 (2006).
- [22] I. Fushman, D. Englund and J. Vuckovic, *Appl. Phys. Lett.* **87**, 241102 (2005).

Chapter 4

Weak exciton-photon coupling between ensemble PbS Quantum dots and silicon photonic crystal cavities and waveguide modes

4.1 Introduction

The study of exciton-photon coupling in chip-scale optical devices is of central interest in the field of cavity QED study in solid-state implementation [1-4]. Colloidal quantum dots (QDs) formed through synthesis in solution such as PbS nanocrystals have emerged as a promising candidate to be integrated on silicon photonic crystal devices working in 1.5 μm [5-7]. Coupling QDs to photonic structures result in a faster recombination rate for the excitons which helps to overcome decoherence issues in the application of single photon source and cavity QED. In the case of weak coupling (the coupling strength between QD and cavity mode is much smaller than their individual decay), the spontaneous emission rates of the excitons are enhanced

by $E = F_p \cdot \left(\frac{\vec{E} \cdot \vec{\mu}}{|\vec{E}_{\text{max}}| |\vec{\mu}|} \right)^2 \cdot \frac{\Delta\lambda_c^2}{\Delta\lambda_c^2 + 4(\lambda - \lambda_c)^2} + F_{phC}$, where $F_p = \frac{3}{4\pi^2} \frac{Q}{V_{\text{eff}}}$ is the ideal

Purcell factor under perfect spectral and spatial alignments and F_{phC} describes the inhibition induced by the photonic band gap [1]. In this Chapter, we experimentally study the weak exciton-photon coupling of PbS quantum dots in air-slot mode-gap cavities which have been demonstrated with high Q and ultra-small mode volume in Chapter 3, and examine the Purcell factor through photoluminescence enhancement and the delayed onset saturation power for QDs coupled to cavity mode.

4.2 Device preparation and micro-photoluminescence

measurement

Air-slot mode-gap cavities discussed in Chapter 3 are fabricated without coupling waveguide for free space micro-photoluminescence (PL) measurement where excitation and collection are in the vertical direction to the sample surface. Before PbS QDs deposition, the device surface is treated with hexamethyl disilazane (HMDS) to make the surface more hydrophobic and improve the uniformity and adhesion of the QDs [8]. By controlling the PbS:chloroform dilution and spin-coat process parameters, approximately 10 μ L of the diluted solution yields an area density of 10³ QDs per μ m² on the surface of photonic crystal cavities. A single layer of PbS QDs is formed on top of the silicon material and even single QD is observable which is highlighted by red circles in the SEM picture shown in Figure 4.1(a). A 980nm laser diode is used as an excitation source with power ~0.5mW before 100X objective lens and emission is collected from a 2 μ m spot near the nanocavity, directed into a grating spectrometer and detected by a liquid N₂ cooled InGaAs array detector. Ensemble PbS QDs we use have a center emission wavelength of 1480nm with a width of 100nm (shown as the inset of Figure 4.1(c) for a high density of QDs) due to a combination of size inhomogeneities and a large homogeneous linewidth at room temperature. PL enhancement is observed at the cavity, compared to a spot slightly away from the cavity where relatively weak background PL signal is observed at the current QD density level. Figure 4.1(b) illustrates the measured PL spectra from air-slot cavities

with different slot widths and air hole radius. Figure 4.1(c) shows the Lorentzian fit of the PL spectrum for the device shown as blue curve in Figure 4.1(b) and the linewidth is 0.39nm with a Q of ~ 3700 . The best Q factor we observed is ~ 5400 , which decreases 3-5 times from the passive cavity transmission measurement in Chapter 3. The cavity Q degradation is mainly due to the roughness and absorption of PbS QDs on the cavity surface and slot edge walls, which can be minimized by lowering the QD density down to $< 10^2$ QDs per μm^2 [9].

4.3 Polarization and power dependent analysis

To examine the polarization property of the PL cavity modes, a polarizer in collection path selects TEx and TEy components out and the collected cavity modes are seen to exhibit strong polarization in TEy direction. A polarization extinction ratio of 5 is inferred from the red and grey curves in Figure 4.2(a). Two PL peaks (separated by 10nm) appear for some devices, and we attribute them to cavity mode II (lower frequency and symmetric shape) and waveguide mode II near slow-light edge (higher frequency and asymmetric shape) which have been discussed already in Chapter 3. When we excite the device from vertical direction in free space, we are more likely to excite waveguide mode II and cavity mode II due to the spatial overlap of these modes with quantum dots, as seen in Figure 4.2(b-c) where magnetic field and electric field energy distributions for cavity mode II and waveguide mode II are

presented. Here waveguide mode near slow-light edge shows similar potential as cavity mode for light-matter interaction [10-11].

In order to further demonstrate the spontaneous emission enhancement due to QD-cavity coupling, a delayed onset of saturation power for QDs coupled to the cavity mode can be used to demonstrate the Purcell effect [12]. A QD coupled well with the cavity mode exhibits a faster radiative recombination rate through the Purcell effect and it should therefore take more photons to saturate the QD (ground state) emission. This approach was chosen instead of a direct QD lifetime measurement due to the low photon counts and higher dark counts in the near-infrared. Figure 4.3 shows excitation power dependences for PL intensities of the cavity mode, waveguide mode near slow-light edge and uncoupled QDs. The ratio between saturation power of cavity/waveguide mode emission and uncoupled QDs is ~ 2 , which indicates that those QDs coupled to cavity mode have enhanced spontaneous emission rates and delayed saturation power. The enhancement factor observed here is an average result from ensemble PbS QDs with imperfect spectral, spatial and polarization alignment to the cavity mode, which is much smaller than the ideal Purcell factor ~ 130 predicted from the measured quality factor of cavity mode II. If working with fewer numbers of QDs on the surface of the slot edge, ideal Purcell factor of up to 3000 is possible with PbS QDs coupled to cavity mode I with $Q \sim 10^4$ which will help to demonstrate the contribution from ultra-small effective mode volume. Here we estimate the emitter-cavity field coupling strength $g = \mu / \hbar \sqrt{\hbar \omega / 2 \epsilon V_{eff}} \sim 20 \text{GHZ}$ [13], and strong coupling is achievable if the air-slot mode-gap photonic crystal cavities possess $Q > 10^4$ and QD

decay can be smaller than the slot cavity decay. Cryogenic temperature environment will help to decrease the nonradiative decay channels of PbS QDs [14]. Slot cavity-colloidal nanocrystal system has great potential to achieve high efficiency single photon source on-demand and even strong exciton-photon coupling in the fiber network communication frequencies.

4.4 Conclusion

In summary, we study the weak exciton-photon coupling of PbS nanocrystals in air-slot mode-gap cavities experimentally. We observed cavity emission $Q \sim 5000$ in photoluminescence measurement with polarization distinction ~ 5 . Average 2 times delayed saturation power for coupled QDs show that spontaneous emission rates are enhanced by cavity mode in air-slot mode-gap photonic crystal cavities. The strongly enhanced light-matter interactions can be used for the application of nonlinear optics, chemical sensor, light emitting device, optical switches and modulators and cavity QED.

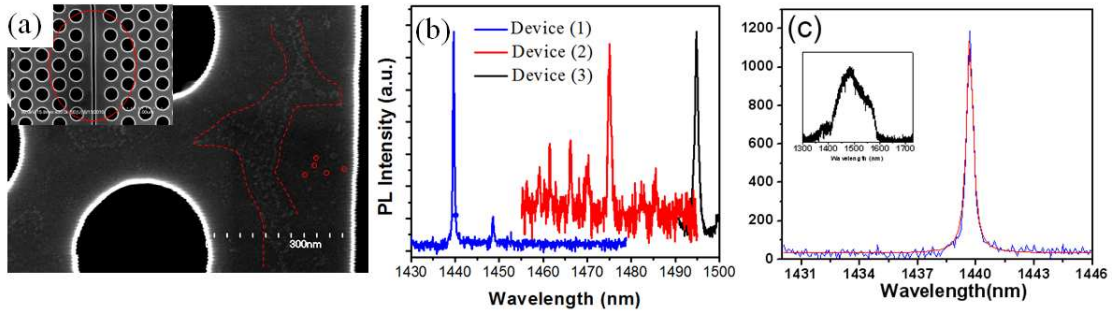


Figure 4.1 (a) SEM picture of the air-slot mode-gap confined cavity with PbS QDs on the surface. The red highlighted region shows the non-uniform QD distribution, and even single PbS QD can be seen clearly. (b) PL spectra of three devices: (blue) $W_0=1.2\times\sqrt{3}a$, $s=120\text{nm}$ and $r=0.296a$; (red) $W_0=\sqrt{3}a$, $s=80\text{nm}$ and $r=0.31a$; (black) $W_0=1.2\times\sqrt{3}a$, $s=100\text{nm}$ and $r=0.324a$. (c) Zoom in and Lorentzian fit of the blue PL spectrum in (b). The inset shows the inhomogeneous PL spectrum from ensemble PbS QDs.

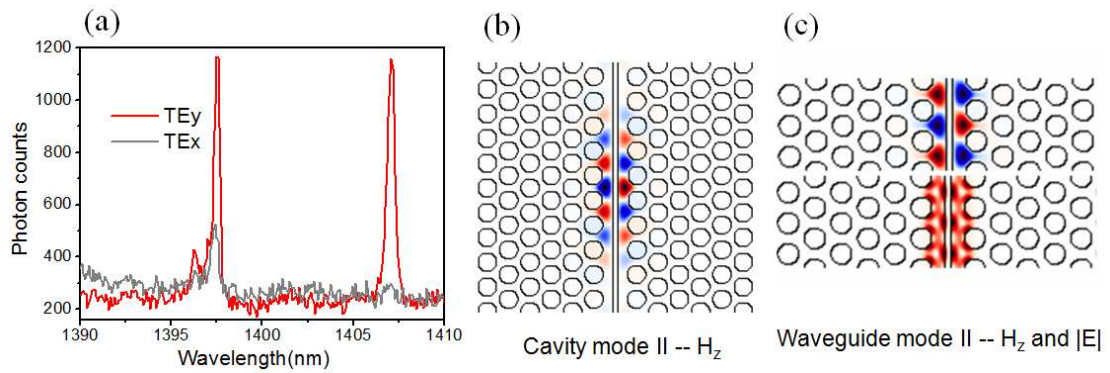


Figure 4.2 (a) PL spectra for TE_x (grey) and TE_y (red) polarization of a particular device in which two resonances are observed. (b) Magnetic field H_z distribution for mode II in air-slot mode-gap cavity. (c) Magnetic field H_z and electric field energy distribution |E| for mode II in air-slot photonic crystal waveguide.

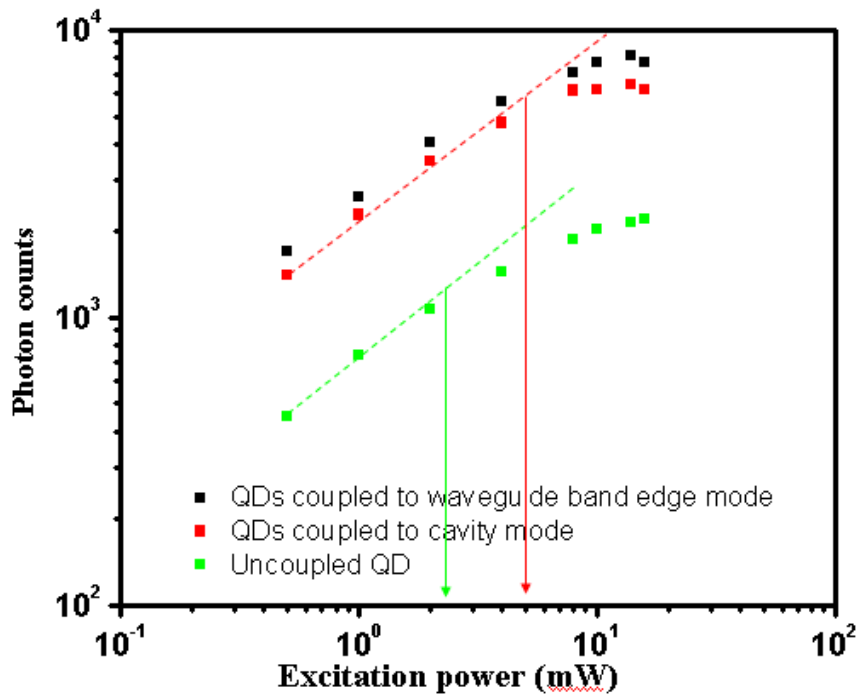


Figure 4.3 Power saturation measurements for QDs coupled to waveguide mode (black), to cavity mode (red) and uncoupled QDs (green). Dashed lines are linear fits before saturation and arrows indicate the excitation powers at the onset of saturation.

Bibliography

- [1] D. Englund, D. Fattal, E. Waks, G. Solomon, B. Zhang, T. Nakaoka, Y. Arakawa, Y. Yamamoto and J. Vuckovic, *Phys Rev Lett* **95** (1) (2005).
- [2] T. Yoshie, A. Scherer, J. Hendrickson, G. Khitrova, H. M. Gibbs, G. Rupper, C. Ell, O. B. Shchekin and D. G. Deppe, *Nature* **432** (7014), 200-203 (2004).
- [3] J. P. Reithmaier, G. Sek, A. Löffler, C. Hofmann, S. Kuhn, S. Reitzenstein, L. V. Keldysh, V. D. Kulakovskii, T. L. Reinecke and A. Forchel, *Nature* **432** (7014), 197-200 (2004).
- [4] E. Peter, P. Senellart, D. Martrou, A. Lemaitre, J. Hours, J. M. Gerard and J. Bloch, *Phys Rev Lett* **95** (6) (2005).
- [5] Fushman, D. Englund and J. Vuckovic, *Appl Phys Lett* **87** (24) (2005).
- [6] R. Bose, X. D. Yang, R. Chatterjee, J. Gao and C. W. Wong, *Appl Phys Lett* **90** (11) (2007).
- [7] R. Bose, J. F. McMillan, J. Gao and C. W. Wong, *Appl Phys Lett* **95** (13) (2009).
- [8] D. V. Talapin and C. B. Murray, *Science* **310** (5745), 86-89 (2005).
- [9] M. T. Rakher, R. Bose, C. W. Wong and K. Srinivasan, *Appl Phys Lett* **96** (16) (2010).
- [10] V. S. C. M. Rao and S. Hughes, *Phys Rev B* **75** (20) (2007).
- [11] E. Viasnoff-Schwoob, C. Weisbuch, H. Benisty, S. Olivier, S. Varoutsis, I. Robert-Philip, R. Houdré and C. J. M. Smith, *Phys Rev Lett* **95** (18), 183901 (2005).
- [12] A. Badolato, K. Hennessy, M. Atature, J. Dreiser, E. Hu, P. M. Petroff and A. Imamoglu, *Science* **308** (5725), 1158-1161 (2005).
- [13] A. Thränhardt, C. Ell, G. Khitrova and H. M. Gibbs, *Phys Rev B* **65** (3), 035327 (2002)
- [14] M. T. Rakher, R. Bose, C. W. Wong and K. Srinivasan, *Opt Express* **19** (3), 1786-1793 (2011).

Chapter 5

**Strong exciton-photon coupling between
single InAs QD and GaAs photonic crystal
waveguide localized mode**

5.1 Introduction

The solid-state cavity quantum electrodynamics (QED) system has been examined as a critical component for quantum information processing, including demonstrations of the single photon source [1], strong coupling [2, 3], two-qubit quantum gate operation [4] and entanglement generation [5]. Generally the prototypical system involves a high quality factor and small mode volume optical cavity, providing a platform to achieve strong coherent interactions between the quantum dot and photon. However, one-dimensional slow-light photonic crystal (PhC) waveguides and surface plasmons waveguides can also be used to increase the local density of states (LDOS) for enhanced light-matter interactions such as spontaneous emission enhancement [6], and furthermore to achieve single photon transistors [7], single photon sources [8] and controlled phase gate [9]. Due to the interference of the coherently scattered light in waveguide devices with unavoidable structural disorder from fabrication, localized modes with high quality factor (Q) have been observed near the slow-light band edge [10, 11]. Recently spontaneous emission control of a single quantum dot (QD) through localization mode (Q up to $\sim 10,000$) in PhC waveguide with engineered disorder has been shown [12]. This PhC waveguide localized mode with a single emitter possesses remarkable possibilities towards efficient single photon sources and controls light-matter interactions in the strong coupling regime for quantum information science. In this Letter, we experimentally study exciton-photon interaction in strong coupling regime with a solid-state device combining the features of a single InAs quantum dot with the attractive properties of GaAs PhC waveguide localized mode. Localized

mode with quality factor ~ 15000 is found near the cutoff of a photonic crystal waveguide mode, and vacuum Rabi splitting is observed when we tune single exciton resonance to be very close to the localized mode resonance. By analyzing the spectra with a complete model [13], we can obtain the experimental parameters for pure dephasing and incoherent pumps. The demonstration of single quantum dot strongly coupled to PhC waveguide localized mode illustrates the strong potential of the system to be used as high efficiency single photon source on-demand or exciton-photon polariton state for quantum computation.

5.2 Optical characterization for a single quantum dot (QD)

5.2.1 Single QD imaging and spectroscopy

Single QD imaging and spectroscopy is the first characterization step before studying the interactions between single QD and chip-scale photonic structures. The samples we use are GaAs wafers with a center layer of InAs QDs grown by molecular beam epitaxy with ultralow density \sim several dots in $20 \mu\text{m}^2$ area. Photoluminescence (PL) measurement in a He-flow cryostat is performed with an above band-gap He-Ne continuous wave laser focused to the sample surface using a $100\times$ microscope objective (NA of 0.75), and the emission light was collected by the same objective, dispersed through a 1m spectrometer and detected with a cooled charged coupled device camera. Figure 5.1 shows the experiment setup and the measured losses for each important optical component. The spectrometer and CCD can be used for either

imaging or spectrum collection by setting the positions of the grating inside the spectrometer. Figure 5.2(a) shows PL from $\sim 10 \mu\text{m}$ by $20 \mu\text{m}$ region on the sample surface when excitation is very high. One bright QD in the center and two weak QDs on the side can be found. By reducing the width and height of the spectrometer entrance slit, a single quantum dot can be selected out and the PL image is shown in Figure 5.2(b). When single QD position is precisely located, we then measure the single exciton line spectrum at 5K with very low excitation power $\sim \text{nW}$ level before objective lens, which shows 0.1nm linewidth as shown in Figure 5.2(c). Please note that for samples with large QD density, single QD may not be observable through imaging if QDs spatial separations are closer than diffraction limit but single exciton lines can be measured under low pump power by spectrometer (40pm resolution for our setup). For the particular sample we use later for device fabrication, QDs density is $\sim 10^2/\mu\text{m}^2$ and they are randomly distributed all over the sample with ensemble emission covering 900-1000 nm range. Figure 5.3(a) and (c) show the narrow single exciton line spectra from two quantum dots on this sample with average excitation power $\sim 1 \mu\text{W}$ before the objective lens. They are excited by He-Ne continuous wave laser and 800nm 80MHz Ti:S 150 fs pulse laser at 9 K and 7 K respectively, and show spectrum linewidth around 0.27 nm and 0.09 nm. The two excitation lasers we use have frequencies above the bandgap of the GaAs material, and the generated electrons and holes will make charges and phonon sidebands of nearby QDs contribute to the spectrum. The effects are more obvious for continuous wave He-Ne laser with current pump power.

5.2.2 Hanbury Brown-Twiss (HBT) measurement

In order to demonstrate the observed narrow spectrum lines are truly emissions from exciton transition in a single quantum dot, Hanbury Brown and Twiss (HBT) measurement is performed to measure the second order coherence function $g^{(2)}$ which describes photon statistics of the emitted photons. This experiment is used to differentiate between states of light and non-classical single emitter source has suppressed coincidence counts at zero time intervals with $g^{(2)}(0) \ll g^{(2)}(\tau)$. We further filter the single exciton line by a high quality 1 nm filter to reduce any undesired background or scattered signals going into the APDs, and then couple the light into a multimode fiber beam splitter which links to two APDs (with time jitter 450ps) and a coincident counter with start and stop channels (shown in Figure 5.1). By measuring probability distribution of the time intervals between photons in a photon stream, we get $g^{(2)}(0) \sim 0.5$ in Figure 5.3(b) and $g^{(2)}(0) \sim 0.28$ in Figure 5.3(d) which reveal the sub-Poissonian distribution property of the single QD emitted photons and are the signatures of a single photon source. We are working with excitation power $\sim 1 \mu\text{W}$ to get enough photon counts from the QD and each HBT measurement takes 40-60mins integration time. As discussed in Ref. [14], the above-band excitation we use here contributes to the remaining value in $g^{(2)}(0)$ in the following ways: (i) excessive electrons and holes are created which can be recaptured by the QD resulting in multi-photon emission; (ii) broad emission surrounding the main emission line (as in Figure 5.3(a)) contaminates the signal, and a narrower bandpass filter will help to reduce

$g^{(2)}(0)$; (iii) background floor in Figure 5.3(d) suggests a long time scale carrier capture process. All these side effects can be avoided by a resonant excitation in future experiment.

5.3 GaAs photonic crystal waveguide localized mode

For photonic crystal waveguide fabrication on a 130nm thick GaAs sample (under the device level is a 650nm AlGaAs sacrificial layer grown on an undoped GaAs substrate) with a center layer of InAs QDs, a compact and efficient 100 kV e-beam writer nB3 is used to define the patterns in the top resist layer. Inductively coupled reactive ion-etching [15] is used to perform GaAs vertical etching. 40s HF wet etching is performed afterwards to create the suspended membrane. Surface roughness, non-uniform air-hole sizes and shape, and pores around air-hole edges are present in our imperfect fabrication processes as shown in Figure 5.4(a). Localized modes could exist in the waveguide near the slow light band edge due to random multiple scattering. Figure 5.4(b) and (c) show the band structure of photonic crystal waveguide and electric/magnetic field distribution of the high order waveguide mode from plane-wave-expansion method calculation. Two slow light regions associated with photonic crystal fundamental mode and high order mode are indicated by the grey boxes and localized mode is observed around the cutoff edge of high order waveguide mode (900-920 nm) in our particular device used for later measurement. 3D simulation

parameters (extracted from SEM measurement) here are: lattice period $a=256\text{nm}$, hole size $r=0.244a$, slab thickness $h=130\text{ nm}$ and PhC waveguide width $W=0.98\sqrt{3}a$.

To characterize localized mode on the waveguide, PL spectrum is collected from the vertical radiation at 40 K with He-Ne continuous wave pump power of 20 μW for two orthogonal polarizations as in Figure 5.5(a), and at 20K with increasing pump power as in Figure 5.5(b). Because of the relatively high power, the spectrum consists of single exciton lines, biexciton lines, localized modes and background QDs emission as indicated in the inset of Figure 5.5(b). Localized mode is highly y-polarized and its peak intensity linearly increases with pump power as shown in Figure 5.5(b), while exciton lines have saturation behavior at high pump power. The single exciton and localized mode examined here have linewidth $\sim 0.06\text{nm}$ at 20 K with pumping power $< 10\mu\text{W}$, which corresponds to quality factor $Q\sim 15,000$.

5.4 Experiment and theoretical analysis of strong exciton-photon coupling

The coupling strength (Rabi frequency) for a quantum dot positioned in a cavity mode

maximum is given by $g = \frac{\mu}{\hbar} \sqrt{\frac{\hbar\omega}{2\epsilon V_{\text{eff}}}}$ where μ is the QD dipole moment and V_{eff} is

the effective cavity mode volume. Generally if the coupling strength is larger than cavity field decay rate Γ_c and emitter decay rate Γ_x , the system is said to be in the strong coupling regime and the system eigenstates are given by the QD-cavity

polariton states, with a distinct splitting spectral signature [16]. However for practical measurement and real device in our case, we have to consider the effect from above band-gap incoherent pumping, QD dephasing, QD blinking, excess carries recaptured by QD or spectral diffusion when temperature and pump power are not low enough. We use the model from Ref. [17] to solve master equation with the following Hamiltonian $H = \frac{1}{2}\hbar\omega_x\sigma_z + \hbar\omega_c a^\dagger a + \hbar g(a^\dagger\sigma_- + a\sigma_+)$ where σ_+ , σ_- and σ_z are the pseudospin operators for two level QD with emitter frequency ω_x , a^\dagger and a are the creation and annihilation operators of photons with cavity frequency ω_c . The incoherent loss and pump terms are included in the master equation of the Lindblad form:

$$d\rho/dt = -i/\hbar[H, \rho] + L(\rho), \text{ and}$$

$$\begin{aligned} L(\rho) = & \frac{\Gamma_x}{2}(2\sigma_- \rho \sigma_+ - \sigma_+ \sigma_- \rho - \rho \sigma_+ \sigma_-) + \frac{P_x}{2}(2\sigma_+ \rho \sigma_- - \sigma_- \sigma_+ \rho - \rho \sigma_- \sigma_+) \\ & + \frac{\Gamma_c}{2}(2a \rho a^\dagger - a^\dagger a \rho - \rho a^\dagger a) + \frac{P_c}{2}(2a^\dagger \rho a - a a^\dagger \rho - \rho a a^\dagger) \\ & + \frac{\gamma_{dep}}{2}(\sigma_z \rho \sigma_z - \rho) \end{aligned} .$$

Here P_x is the rate in which excitons are created by the continuous wave pump laser, P_c is the incoherent pumping of the cavity mode [18] and γ_{dep} is the pure dephasing rate of the exciton. Effective decay rates can be defined as $\Gamma_x' = \Gamma_x + 2\gamma_{dep} + P_x$, $\Gamma_c' = \Gamma_c - P_c$ and strong coupling can be achieved if $g > \Gamma_x'/4, \Gamma_c'/4$ [13]. We assume the collected light is mostly from cavity at steady

state $\sim \int_0^\infty e^{-i(\Gamma_r - \omega)\tau} \langle a^\dagger(t)a(t+\tau) \rangle d\tau$ where Γ_r is our system spectral resolution ~ 7 GHZ.

Please note that effects such as QD blinking [19], cavity decay [20, 21], background excitons or spectral diffusion are not included in the master equation above but indeed contribute to experimental spectra when temperature and above-band pump are not low enough, so we have included these effects in the calculated spectra (solid curves in Figure 5.6(a)) to explain the extra peak or asymmetric spectrum when we compare with experimental spectra at different temperature with pump power level $\sim 7 \mu\text{W}$ before the objective lens (open circles in Figure 5.6(a)). Frequency detuning between the exciton line and localized mode is -0.04nm at beginning $T = 26 \text{ K}$. When device temperature is scanned from 26 K to 29.5 K , QD emission wavelengths strongly redshift ($\sim 0.23\text{nm}$) as the temperature increases due to band gap shrinkage and the cavity wavelength shift rate is 10 times slower. In this case, the frequency detuning between QD and localized mode can be continuously tuned across zero point and further into positive side when temperature increases. Vacuum Rabi splitting $\sim 0.216 \text{ nm}$ is observed when QD is on resonant with the localized mode $\sim 915.255 \text{ nm}$ at 27 K . Figure 5.6(b) shows the resonances of two polariton peaks (red and black dots) extracted from experimental spectra and theoretical fitting (red and black curve for a larger temperature range) as a function of temperature. Blue dash lines represent uncoupled cavity and QD resonances as guideline curves, from which we can see that the on resonant case happens at 27 K and the trend of anti-crossing behavior in polariton resonances is shown as expected but limited by our temperature scanning range. From the theoretical fittings, we can extract the coupling strength $g \sim 39 \text{ GHz}$,

pure dephasing rate $\gamma_{dep} \sim 10\text{-}20$ GHz, incoherent cavity pump rates $P_c \sim 5\text{-}15$ GHz and incoherent exciton pump rates $P_x \sim 15$ GHz. $\Gamma_x \sim$ sub GHz is used for InAs QDs with ns radiation lifetime. The coupling strength g here is larger than previous values got from QD in photonic crystal defect type cavities [2] which might be caused by better spatial overlap between QD and waveguide localized mode with smaller effective mode volume, but it is still smaller than the best device reported so far is in Ref. [20]. Compared with the decay rates in our device, strong coupling condition is satisfied. We have also experienced dephasing rate and incoherent cavity pump rate increases with temperature which is evidence for decoherence mediated by coupling to acoustic phonons [22-23] and cavity feeding mediated by electron-acoustic phonon scattering [24].

5.5 Conclusion

In conclusion, we experimentally showed that strong exciton-photon coupling can be achieved between single InAs quantum dot and localized mode in photonic crystal waveguide. By comparing with theoretical model in which pure dephasing, cavity pumping and exciton pumping are considered, we analyze the contributions coming from the above-band pump laser and non-zero temperature in our experiment. The results confirm that strong coupling does not always appear as a symmetric mode splitting spectrum [25] but highly depends on the experimental parameters. Furthermore to prove the quantum nature of the strong coupling system, photon correlation or photon blockade measurements [26] are needed. The localized mode in

photonic crystal waveguide we observed is near the slow-light region and could be due to Anderson localization, and multiple localized modes have been observed for long waveguides with length $\sim 80\mu\text{m}$ [12]. Large scale arrays of localized modes with the inherently efficient input-output coupling can be achieved, and their strong coupling to single QDs opens the doors to an interesting and promising cavity QED system which favors the scalability requirement for on-chip single photon source, entanglement generation and quantum information processing.

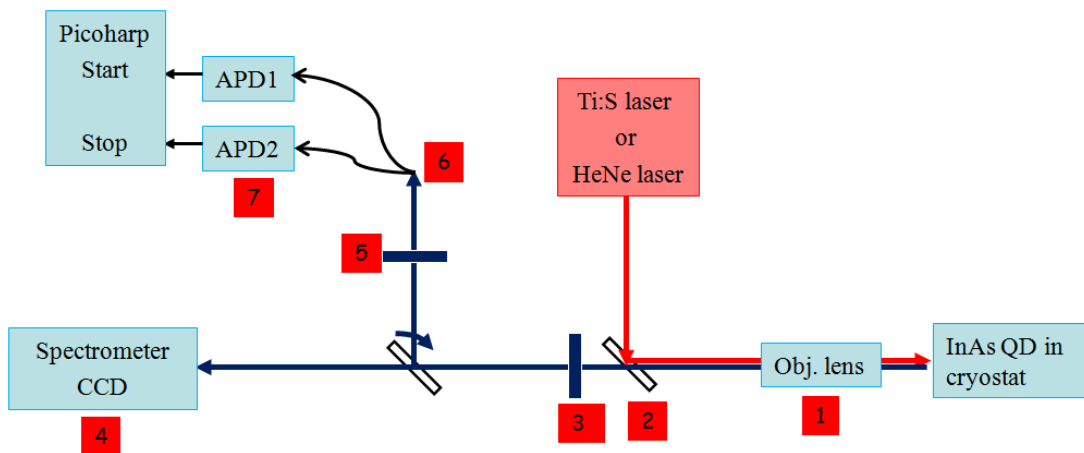


Figure 5.1 Experiment setup for single quantum dot spectroscopy and HBT measurement. Collection efficiency is 0.8% (-21dB) for spectrum and 0.2% (-27dB) for correlation measurement. Losses due to each component are list as below:

1. Obj. lens NA 0.7 ~ 7%
2. Beam splitter ~50%
3. HP filter ~ 90%
4. Grating ~ 55% and CCD ~50%
5. Bandpass filter 1nm ~50%
6. Fiber coupling ~ 60%
7. APD coupling ~ 90% and APD efficiency at 920nm ~ 25%

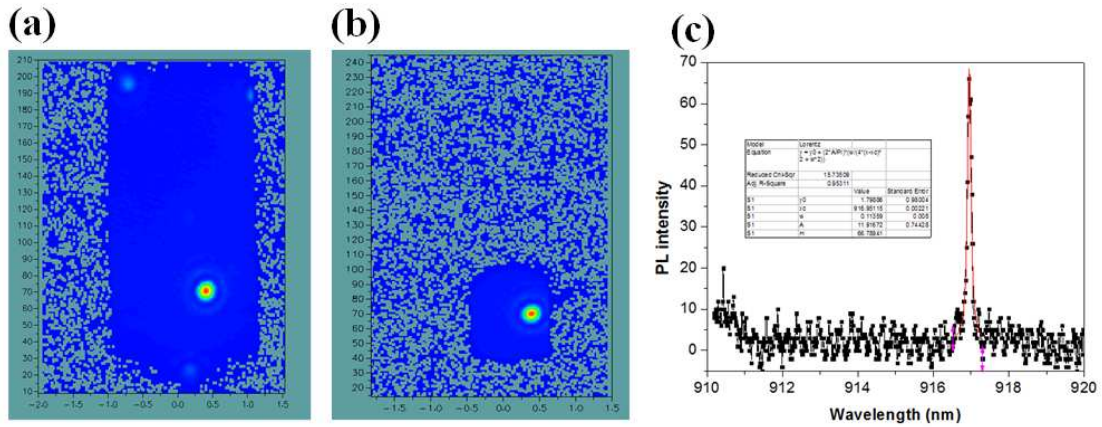


Figure 5.2 (a-b) Single quantum dot imaging on cooled Si CCD of a sample with ultralow QD density. A single quantum dot can be selected by narrowing the entrance slit of the spectrometer. **(c)** PL spectrum from a single QD in (b) under very low CW He-Ne excitation.

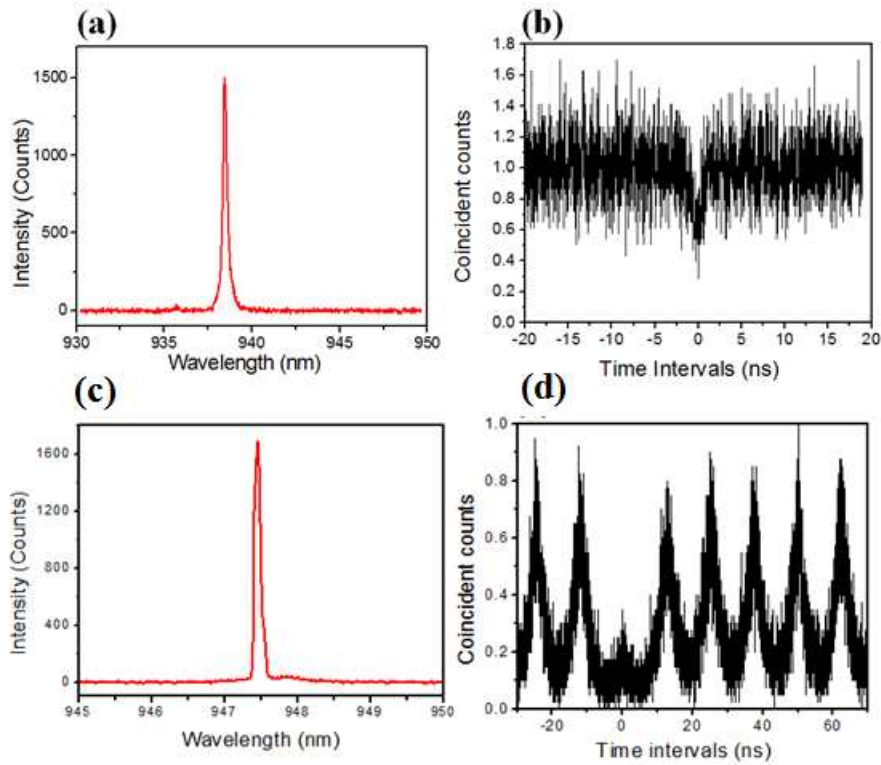


Figure 5.3 (a) (b) A single QD exciton line spectrum and HBT measurement under continuous wave laser excitation at 9K. The normalized coincidence counts at time interval zero is ~ 0.5 . (c) (d) A single QD exciton line spectrum and HBT measurement under pulsed laser excitation. The normalized coincidence counts at time interval zero is ~ 0.28 .

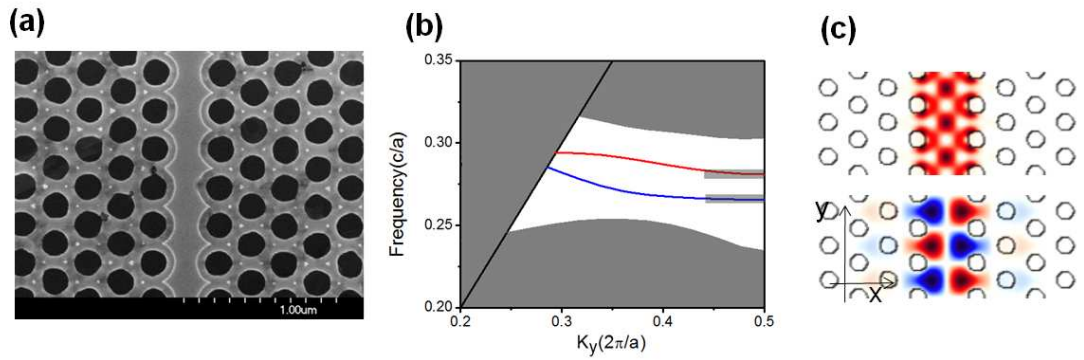


Figure 5.4 (a) A scanning electron microscope (SEM) image of a fabricated PhC waveguide (b) Band structure for PhC waveguide used in experiment. Red and blue lines indicate the high order and fundamental waveguide modes, and the red box shows the slow light region where localized modes are expected. (c) Electric field energy $|E|^2$ (top) and magnetic field H_z (bottom) distributions for high order waveguide mode near slow light region.

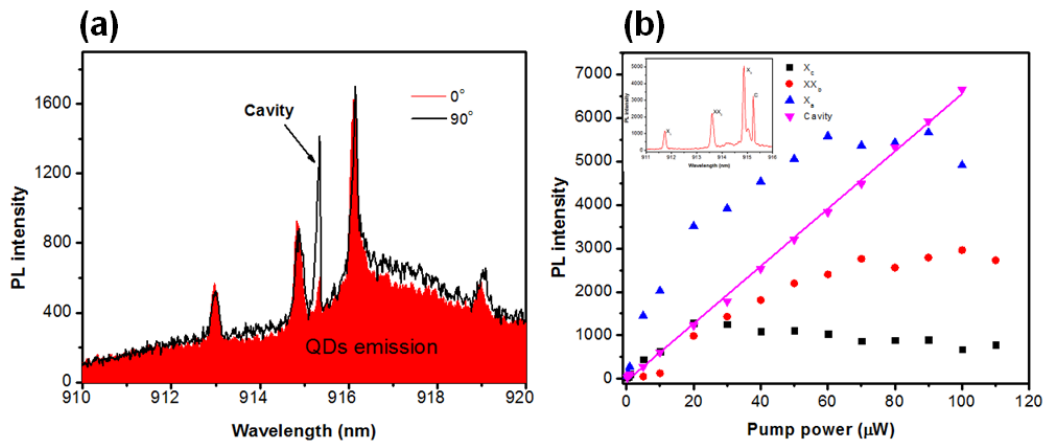


Figure 5.5 (a) Polarization dependence measurements of the QDs and localized mode when $T = 40$ K with high excitation power $\sim 20 \mu\text{W}$. (b) Power dependence measurements of the QDs and localized mode when $T = 20$ K.

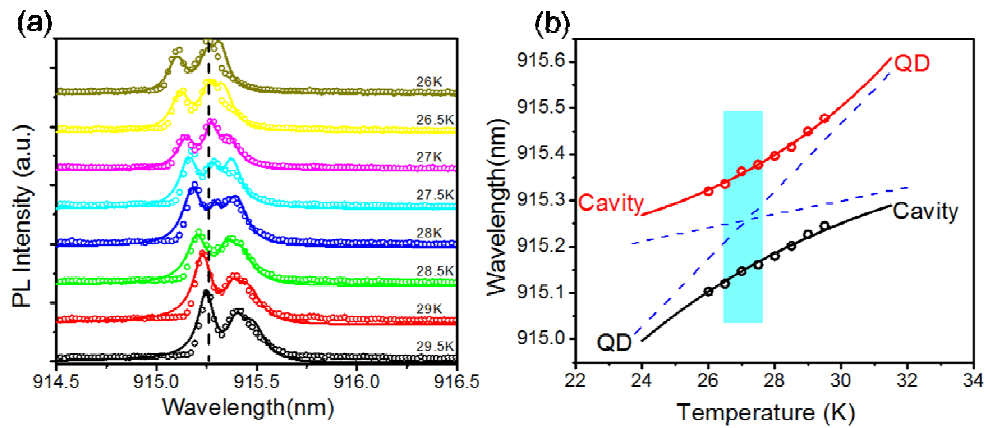


Figure 5.6 (a) Experimental spectra (open circles) and calculated spectra (solid curves) of the coupled system when temperature is scanned from 26 K to 29.5 K. (b) Resonances of two polariton peaks extracted from experimental spectra (red and black dots) and theoretical fitting (red and black curve for a larger temperature range) as a function of temperature. Blue dash lines represent uncoupled cavity and QD resonances as guideline curves.

Bibliography

- [1] P. Michler, A. Kiraz, C. Becher, W. V. Schoenfeld, P. M. Petroff, L. D. Zhang, E. Hu and A. Imamoglu, *Science* **290** (5500), 2282-+ (2000).
- [2] A. Imamoglu, K. Hennessy, A. Badolato, M. Winger, D. Gerace, M. Atature, S. Gulde, S. Falt and E. L. Hu, *Nature* **445** (7130), 896-899 (2007).
- [3] D. Englund, A. Faraon, I. Fushman, N. Stoltz, P. Petroff and J. Vuckovic, *Nature* **450** (7171), 857-861 (2007).
- [4] L. M. Duan and H. J. Kimble, *Phys Rev Lett* **92** (12) (2004).
- [5] E. Waks and J. Vuckovic, *Phys Rev Lett* **96** (15) (2006).
- [6] E. Viasnoff-Schwoob, C. Weisbuch, H. Benisty, S. Olivier, S. Varoutsis, I. Robert-Philip, R. Houdré and C. J. M. Smith, *Phys Rev Lett* **95** (18), 183901 (2005).
- [7] D. E. Chang, A. S. Sorensen, E. A. Demler and M. D. Lukin, *Nat Phys* **3** (11), 807-812 (2007).
- [8] V. S. C. M. Rao and S. Hughes, *Phys Rev Lett* **99** (19) (2007).
- [9] J. Gao, F. W. Sun and C. W. Wong, *Appl Phys Lett* **93** (15) (2008).
- [10] S. Mookherjea, J. S. Park, S. H. Yang and P. R. Bandaru, *Nat Photonics* **2** (2), 90-93 (2008).
- [11] J. Topolancik, B. Ilic and F. Vollmer, *Phys Rev Lett* **99** (25), 253901 (2007).
- [12] L. Sapienza, H. Thyrrerstrup, S. Stobbe, P. D. Garcia, S. Smolka and P. Lodahl, *Science* **327** (5971), 1352-1355 (2010).
- [13] E. del Valle, F. P. Laussy and C. Tejedor, *Phys Rev B* **79** (23) (2009).
- [14] C. Santori, D. Fattal, J. Vuckovic, G. S. Solomon and Y. Yamamoto, *New J Phys* **6** (2004)
- [15] S. Combrie, S. Bansropun, M. Lecomte, O. Parillaud, S. Cassette, H. Benisty and J. Nagle, *J Vac Sci Technol B* **23** (4), 1521-1526 (2005).

- [16] T. Yoshie, A. Scherer, J. Hendrickson, G. Khitrova, H. M. Gibbs, G. Rupper, C. Ell, O. B. Shchekin and D. G. Deppe, *Nature* **432** (7014), 200-203 (2004).
- [17] A. Laucht, N. Hauke, J. M. Villas-Boas, F. Hofbauer, G. Bohm, M. Kaniber and J. J. Finley, *Phys Rev Lett* **103** (8) (2009).
- [18] D. Press, S. Gotzinger, S. Reitzenstein, C. Hofmann, A. Löffler, M. Kamp, A. Forchel and Y. Yamamoto, *Phys Rev Lett* **98** (11) (2007).
- [19] A. Reinhard *et al.*, <http://arxiv.org/abs/1108.3053>.
- [20] M. Winger, A. Badolato, K. J. Hennessy, E. L. Hu and A. Imamoglu, *Phys Rev Lett* **101** (22) (2008).
- [21] S. Hughes and P. Yao, *Opt Express* **17** (5), 3322-3330 (2009).
- [22] I. Favero, A. Berthelot, G. Cassabois, C. Voisin, C. Delalande, P. Roussignol, R. Ferreira and J. M. Gérard, *Phys Rev B* **75** (7), 073308 (2007).
- [23] I. Favero, G. Cassabois, R. Ferreira, D. Darson, C. Voisin, J. Tignon, C. Delalande, G. Bastard, P. Roussignol and J. M. Gérard, *Phys Rev B* **68** (23), 233301 (2003).
- [24] S. Hughes, P. Yao, F. Milde, A. Knorr, D. Dalacu, K. Mnaymneh, V. Sazonova, P. J. Poole, G. C. Aers, J. Lapointe, R. Cheriton and R. L. Williams, *Phys Rev B* **83** (16), 165313 (2011).
- [25] M. O. Scully *et al.*, *Quantum Optics* (Cambridge University Press, Cambridge, 1997).
- [26] A. Faraon, I. Fushman, D. Englund, N. Stoltz, P. Petroff and J. Vuckovic, *Nat Phys* **4** (11), 859-863 (2008).

Chapter 6

Quantum controlled phase gate through a single quantum dot in a slow-light photonic crystal waveguide

6.1 Introduction

The atom-cavity system has been examined as a critical component for quantum information processing, including demonstrations of the single photon source [1], two-qubit quantum gate operation [2-3], and entanglement generation [4]. Generally the prototypical system involves a high quality factor and small mode volume optical cavity, providing a platform to achieve strong coherent interactions between the atom and photon. Using a cavity to modify the local density of states (LDOS), however, the qubit operation is typically limited to a narrow-band spectral region, in addition to photon extraction, scalability and integrability issues that need to be carefully considered. Alternatively, other possible mesoscopic structures to increase the LDOS include one-dimensional slow-light photonic crystal (PhC) waveguides [5] and surface plasmons waveguides. Such systems have been theoretically proposed recently to achieve single photon transistors and single photon sources [6, 7]. Remarkable observations such as enhanced spontaneous emission [8] and strong coupling seen in mesoscopic microcavities can also be ported into the PhC waveguide or nanowire system. For instance, signatures of spontaneous emission enhancement with ensemble QDs in a PhC waveguide have recently been observed [9]. In this Chapter, we propose a system which consists of photonic crystal waveguides and low dimensional semiconductor QD for implementing the controlled phase-flip (CPF) gate between two flying qubits. This two-qubit phase gate, together with single-bit rotations, is sufficient for universal quantum computation. Our proposed system makes use of the tight optical confinement and low group velocity of waveguide modes to influence the

emission of a QD localized inside the standard PhC waveguide. By controlling the QD's quantum state, we demonstrate the correlated phase control of the transport property of the system and implement quantum information processing for qubits coded as superposition states of single photon's polarizations. We further show that enhanced quantum dots emission into photonic crystal waveguide mode provides high gate fidelity over broadband frequencies. Moreover, excitation of waveguide mode and extraction of quantum dot emission are extremely efficient in this system, and chip-scale integration is possible.

6.2 Transport property for PhC waveguide embedded with a single QD

For a PhC W1 (with one missing line of holes) waveguide, the dispersion diagram of the fundamental TE-like propagation mode is shown in Figure 6.1(a). A divergent-like LDOS and slow group velocity for the fundamental propagating waveguide mode is seen for wavelengths near the PhC waveguide mode cut-off edge (at $0.266 (c/a)$, where c is the vacuum speed of light and a is the lattice constant of photonic crystal). Emission of an emitter embedded in a PhC waveguide, at the field maximum of the localized waveguide mode, exhibits a large spontaneous emission enhancement proportional to $1/(v_g V_{eff})$, where v_g is the group velocity and V_{eff} the effective mode volume per unit cell for a PhC waveguide fundamental mode. Furthermore, a large propagation mode β factor – probability of a photon being emitted into a desired

waveguide mode regardless of non-radiative decay of the emitter – is obtained throughout the entire propagation spectrum [7]. Figure 6.1(b) shows a schematic diagram of the system, with a three-level emitter. The ground and excited states, $|g\rangle$ and $|e\rangle$ respectively, are coupled via h -polarization photons (corresponding to the waveguide TE mode) with frequency ω_{wg} . A metastable state $|s\rangle$ is decoupled from waveguide modes but is resonantly coupled to $|e\rangle$ via a classical, optical control field with Rabi frequency $\Omega(t)$. Dynamics of the emitter operator σ_- is described by Heisenberg operator equation

$$\frac{d\sigma_-}{dt} = -\frac{1}{2\tau}\sigma_- + i\delta_{\text{ew}}\sigma_- + \kappa a_{\text{in}} \quad (6.1)$$

where a_{in} (b_{in}) is the field operator for the flux of the waveguide input port. The waveguide output fields a_{out} and b_{out} are related to the input fields by $a_{\text{out}} = a_{\text{in}} + \kappa\sigma_-$ and $b_{\text{out}} = b_{\text{in}} + \kappa\sigma_-$. $1/\tau = 1/\tau_{\text{SE}} + 1/\tau_{\text{NR}} + 1/\tau'$ is the total decay rate of the emitter, in which $1/\tau_{\text{SE}} = PF/\tau_0$ is the emitter's spontaneous emission rate in the PhC waveguide (where PF is the Purcell factor and $1/\tau_0$ is the emitter decay rate in bulk material), $1/\tau_{\text{NR}}$ is the nonradiative decay rate and $1/\tau'$ is related to the spontaneous emission into a continuum of radiation and/or leaky modes. δ_{ew} and κ are respectively the frequency detuning and coupling coefficient between emitter and waveguide mode, and $\kappa = 1/\sqrt{2\tau_{\text{SE}}}$. We use the calculated β factors in Ref. [7] (defined as

$\beta = \frac{1/\tau_{\text{SE}}}{1/\tau_{\text{SE}} + 1/\tau'}$ and examined to be greater than 0.9 for ideal polarization match) and

consider the QD τ_0 to be 1 ns, and the nonradiative decay to be sub-GHz at low temperature [10]. Figure 6.1(c) shows the reflectance $R (=|r|^2 = |b_{out}/a_{in}|^2)$ as a function of detuned quantum dots transition to the normalized frequency of waveguide mode. The waveguide frequencies f are normalized to c/a and are examined for $f = 0.2662, 0.2668, 0.2682$ and 0.2827 . Figure 6.1(c) shows that the reflectance curve is spectrally broadened with maximum reflectance close to unity when the waveguide mode approaches slower group velocities. Nonradiative recombination of the quantum dot as a loss mechanism is also shown here for the case of $\tau_{NR} = \tau_0$, where the maximum reflectance peak is decreased for increased non-radiative recombination rates. The inset of Figure 6.1(c) shows numerically calculated reflection coefficient (both real and imaginary parts) and phase when $f = 0.2662$. It indicates that $r \approx -1$ when the QD is on resonance with the waveguide mode with a slow group velocity of $\sim c/154$. An input photon is nearly perfectly reflected by the single QD, and simultaneously gets a π -phase shift. Similar reflection properties have also suggested in surface plasmons nanowires [6], and Ref. [11] describes the ideal waveguide case. Existing losses during the photon-emitter interaction come from two aspects: quantum dot dephasing processes and non-unity β factors. We also emphasize the analogy of the reflectance character to that of an unloaded cavity-waveguide system [12], where detuning away from the slow-light mode cutoff edge unloads the coupled QD-PhC waveguide system towards only the intrinsic QD linewidth.

6.3 Construction scheme for quantum controlled phase gate

Based on the QD-PhC waveguide system described above, we can adopt Duan's protocol (see Ref. [3]) in which a CPF gate is implemented by sequential injection of two single photons, together with single qubit rotations. However, here we consider a more compact schematic setup as shown in Figure 6.2(a) to realize a CPF gate between input photon A (target qubit) and input photon B (control qubit). Generally the input photon state A or B can be described as $(|h\rangle + |v\rangle)/\sqrt{2}$ and, after the polarization beam splitter (PBS), only $|h\rangle_A$ mode or $|h\rangle_B$ mode enters at the 50:50 beam splitter (BS) and couples into the PhC waveguide from both sides simultaneously. In PhC waveguide, the single photon state is a superposition of the left- and right- propagation waveguide mode. After traveling through the Sagnac loop, the photon recombines at the BS and exits the system from the same port it entered. Moreover, using the 50:50 BS transformation matrix [13], the $|h\rangle_A$ mode and $|h\rangle_B$ mode will gain a π -phase difference with respect to each other when they leave the Sagnac loop and we denote this effect as $|h\rangle_A \xrightarrow{\text{Sagnac}} |h\rangle_A, |h\rangle_B \xrightarrow{\text{Sagnac}} -|h\rangle_B$. We note that the optical paths and propagation loss for $|h\rangle$ and $|v\rangle$ components can be stably tuned experimentally to be identical. All these free space light paths can also be

integrated onto a single chip. When the emitter is on ground state, $|h\rangle_A$ coming from port A will get a π -phase shift after reflection by QD and leaves our system as $-|h\rangle_A$.

The implementation of the CPF gate between photon A and B thereby consists of three steps in the protocol. We first show, in ideal case, the initial and final states of the QD-photon system to illustrate the states evolution after each step of the CPF protocol:

(I) First we initialize the emitter in ground state and apply a control field $\Omega(t)$ simultaneous with the arrival of single photon B. The control field (properly chosen to be impedance matched [14]) will result in capture of the incoming single photon while inducing QD state flips from $|g\rangle$ to $|s\rangle$:

$$|h\rangle_B |g\rangle_{QD} \rightarrow |vac\rangle_B |s\rangle_{QD}, |v\rangle_B |g\rangle_{QD} \rightarrow |v\rangle_B |s\rangle_{QD}, \quad (6.2)$$

where we used $|vac\rangle_B$ to describe the h -polarized B photon after storage.

(II) Next we send photon A into the system. Only when emitter is on ground state $|g\rangle$ will the QD-waveguide system reflect photon $|h\rangle_A$ and introduce a π -phase shift on this photon simultaneously. The whole system will result in four possible states as below:

$$\begin{aligned} |h\rangle_A |vac\rangle_B |s\rangle_{QD} &\rightarrow |h\rangle_A |vac\rangle_B |s\rangle_{QD}, |v\rangle_A |vac\rangle_B |s\rangle_{QD} \rightarrow |v\rangle_A |vac\rangle_B |s\rangle_{QD}, \\ |h\rangle_A |v\rangle_B |g\rangle_{QD} &\rightarrow -|h\rangle_A |v\rangle_B |g\rangle_{QD}, |v\rangle_A |v\rangle_B |g\rangle_{QD} \rightarrow |v\rangle_A |v\rangle_B |g\rangle_{QD} \end{aligned} \quad (6.3)$$

(III) Finally we can choose the same $\Omega(-t)$ to drive the emitter from $|s\rangle$ back to $|g\rangle$, and retrieve single photon $|h\rangle_B$ as a time reversal process of (I). The retrieval process can be expressed as $|\text{vac}\rangle_B |s\rangle_{\text{QD}} \rightarrow |h\rangle_B |g\rangle_{\text{QD}}$. The retrieval photon generated in PhC waveguide is exactly the same as the input photon in (I), but it will get a π -phase change when it leaves the BS.

$$\begin{aligned} |h\rangle_A |\text{vac}\rangle_B |s\rangle_{\text{QD}} &\rightarrow -|h\rangle_A |h\rangle_B |g\rangle_{\text{QD}}, |v\rangle_A |\text{vac}\rangle_B |s\rangle_{\text{QD}} \rightarrow -|v\rangle_A |h\rangle_B |g\rangle_{\text{QD}}, \\ -|h\rangle_A |v\rangle_B |g\rangle_{\text{QD}} &\rightarrow -|h\rangle_A |v\rangle_B |g\rangle_{\text{QD}}, |v\rangle_A |v\rangle_B |g\rangle_{\text{QD}} \rightarrow |v\rangle_A |v\rangle_B |g\rangle_{\text{QD}} \end{aligned} \quad (6.4)$$

After these three steps, the state of input photons can thus be described by:

$$\begin{aligned} |\varphi\rangle_{\text{initial}} &= |h\rangle_A |h\rangle_B + |v\rangle_A |h\rangle_B + |h\rangle_A |v\rangle_B + |v\rangle_A |v\rangle_B \\ \Rightarrow |\varphi\rangle_{\text{ideal}} &= -|h\rangle_A |h\rangle_B - |v\rangle_A |h\rangle_B - |h\rangle_A |v\rangle_B + |v\rangle_A |v\rangle_B \end{aligned} \quad (6.5)$$

This ideal photon states evolution demonstrates the completed implementation of controlled phase flip gate operation, which preserves the final phase of A and B photons relative to input only when they are both in v polarization, otherwise the final phase will get a π -phase change. The emitter is not entangled with the photon states and returns to the original ground state after the gate operation.

6.4 Gate fidelity and photon loss analysis

We emphasize the importance of the Sagnac loop in our scheme. Because the PhC waveguide is a two-side coupling system (QD emission couples into both left- and right- propagation waveguide modes), if we have incident $|h\rangle_A$ mode only from one

side of the waveguide in step (II) (the QD state at the end of step (I) can be $|g\rangle$ or $|s\rangle$), we will get both transmitted and reflected modes after the interaction. We cannot combine these two modes later into a single output without loss because they are entangled with the QD. The advantage of using Sagnac loop here is to remove the entanglement between the waveguide left- and right-propagating modes and the QD, by having $|h\rangle_A$ mode incident from both sides of the waveguide. Thus we can get single output $-|h\rangle_A$ (when QD state is $|g\rangle$) or $|h\rangle_A$ (when QD state is $|s\rangle$).

Furthermore we discuss the storage and retrieval process in step (I) and (III). We need coherent storage and retrieval of a single photon $|h\rangle_B$ and the store/retrieval efficiency degrades the quality of the control phase gate. In our case, the optimal storage strategy in (I) is splitting the incoming pulse and having it incident from both sides of the emitter simultaneously, which is the time reversal process of a single photon generation. There is a one-to-one correspondence between the incoming pulse shape and the optimal field $\Omega(t)$. The retrieval process in (III) is time reversal process of the storage process in (I) and both efficiencies are theoretically determined by the calculated reflection/transmission coefficient [6, 15]. Reversible transfer of coherent light to and from the internal state of a single trapped atom in a cavity has already been demonstrated in experiment [16] and the efficiency could improve up to 90%.

Next we consider non-ideal cases which include frequency mismatch between emitter and waveguide mode, nonradiative decay of the emitter, experimentally achievable values of low group velocities, as well as photon storage and retrieval

efficiency. We include in Figure 6.2(b) all the above loss mechanisms and experimental limitations into the photon loss during the gate operation. Not surprisingly the gate loss decreases to very low level when we operate at the slow-light PhC waveguide frequencies and the gate loss increases when the non-radiative decay of the quantum dot is comparable to the radiative decay. Fidelity of the CPF gate, described by $|\langle \varphi_{ideal} | \varphi_{actual} \rangle|$, measures the difference between the actual output photon state and the ideal [Eqn. (5)] state. We note that the PhC waveguide mode propagation loss and the insertion loss (when light is coupled into and extracted from PhC waveguide) do *not* decrease the gate fidelity. Figure 6.2(c) shows how the QD-waveguide CPF gate fidelity changes with normalized frequency detuning $\delta_{ew} / (1/\tau_0)$ and waveguide mode frequency ω_{wg} . In addition, in Figure 6.2(c), the decrease of the gate fidelity with increasing frequency mismatch indicates the requirement of the input photon frequency (waveguide mode frequency) to be on-resonant with the quantum dot transition. However, the frequency matching here is not as stringent as the cavity cases because of the broad spectral range of the propagating PhC waveguide mode. Figure 6.2(d) shows the QD-waveguide CPF gate fidelity as a function of PhC waveguide mode frequencies (on resonance with QD). When $f = 0.2662$, $v_g \approx c/154$ have been measured experimentally [17]. Spontaneous emission rate is enhanced by $PF = 30$ and leads to β factor nearly 0.998 for a QD located at the field antinodes with the same dipole orientation as the mode polarization [7]. The reflectance peak is as high as 0.988 and leads to a gate fidelity up to 0.9999

with $\tau_{\text{NR}} = 10\tau_0$ used in the simulations. When $f = 0.2827$, the PF tends towards 1 with normal waveguide group velocity yet gate fidelity remains above 0.96. Although the Purcell factor is very low in this case, the reason of the high fidelity is that the QD emissions into free space or other leaky modes are highly suppressed inside the photonic crystal band gap and the one-dimensional waveguide, and thus we have a large β factor (> 0.9) maintained throughout the waveguide mode spectral range ($\sim 10\text{THz}$ from Figure 6.1(a)). Compared with cavity-assisted schemes in which Lorentzian shape resonance features are involved, the gate operation bandwidth in waveguide-assisted system is much larger. For example, as long as the QD transition is within $\sim 2\text{THz}$ (15nm) above the waveguide cut-off frequency, our scheme always gets fidelity greater than 0.99 as well as gate loss smaller than 0.18. Moreover even with a quantum dot with 50% quantum yield ($\tau_{\text{NR}} = \tau_0$), the gate fidelity still remains higher than 0.9 within $\sim 2\text{THz}$ bandwidth. This is because of the Purcell-enhanced QD spontaneous emission rate into the waveguide mode. For QDs with even lower quantum efficiency, the gate fidelity stays above 90% only when we operate close to the slow-light edge, and obviously decreases quickly. In this case, schemes with ultrahigh Q cavities will benefit from the larger Purcell factors, reducing the effect of QD's nonradiative decay, but at the expense of cavity-limited bandwidth. Combining the contribution both from Purcell factor and large β factor, our QD-PhC waveguide system has a distinctive advantage compared to cavity-assisted schemes by relaxing the frequency matching condition (frequency match between quantum dot transition and cavity resonance) by \sim two orders of magnitude or more. We can also take

advantage of this broad bandwidth to offset the actual experimental slow-light propagation and coupling losses by operating slightly away from the slowest group velocity regions for acceptable gate fidelity and gate loss.

6.5 Conclusion

In summary we have proposed a scheme to realize quantum control phase-flip gate between two photons through photon-QD interaction in a photonic crystal waveguide. Strong optical confinement and low group velocity in photonic crystal waveguide contributes to the high gate fidelity (~ 0.99) over a tremendous broadband region ($\sim 2\text{THz}$). In our scheme, excitation and extraction can be extremely efficient and chip-scale integration is possible. All these advantages show QD-photonic crystal waveguide system is very promising to be a critical component in quantum information processing.

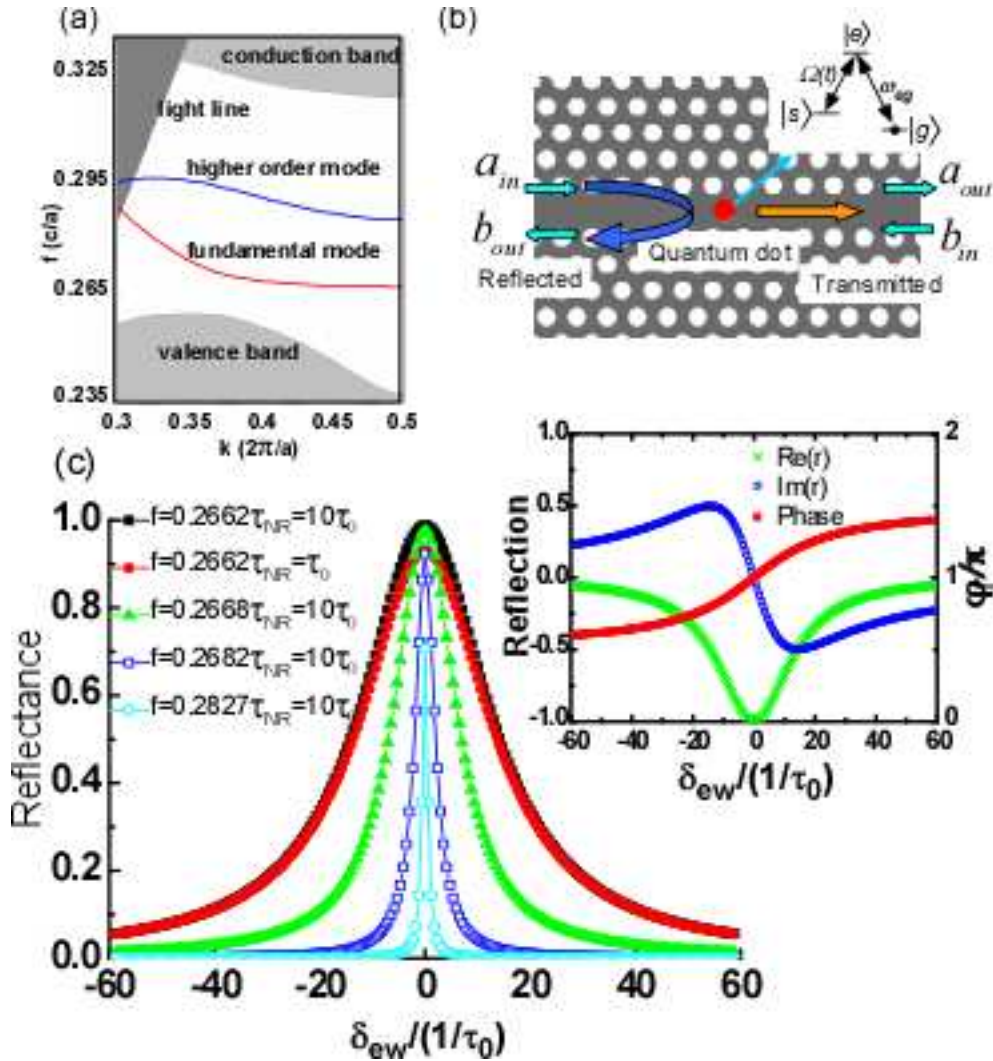


Figure 6.1 (a) PhC waveguide band structure within the TE-like band gap. Both fundamental (red) and a higher order mode (blue) are shown. Structure parameters: $r = 0.275a$, $h = 0.5a$, $\epsilon = 12$ and $a = 420\text{nm}$. (b) Schematic diagram of a single incident photon interacts with a near resonant QD. (c) Reflectance as a function of normalized quantum dot detuning frequencies for different normalized PhC waveguide frequencies with quantum dot $\tau_{NR} = 10\tau_0$ and $\tau_{NR} = \tau_0$. Inset: Reflection coefficient (real part and imaginary part) and phase when $f = 0.2662$, $\tau_{NR} = 10\tau_0$.

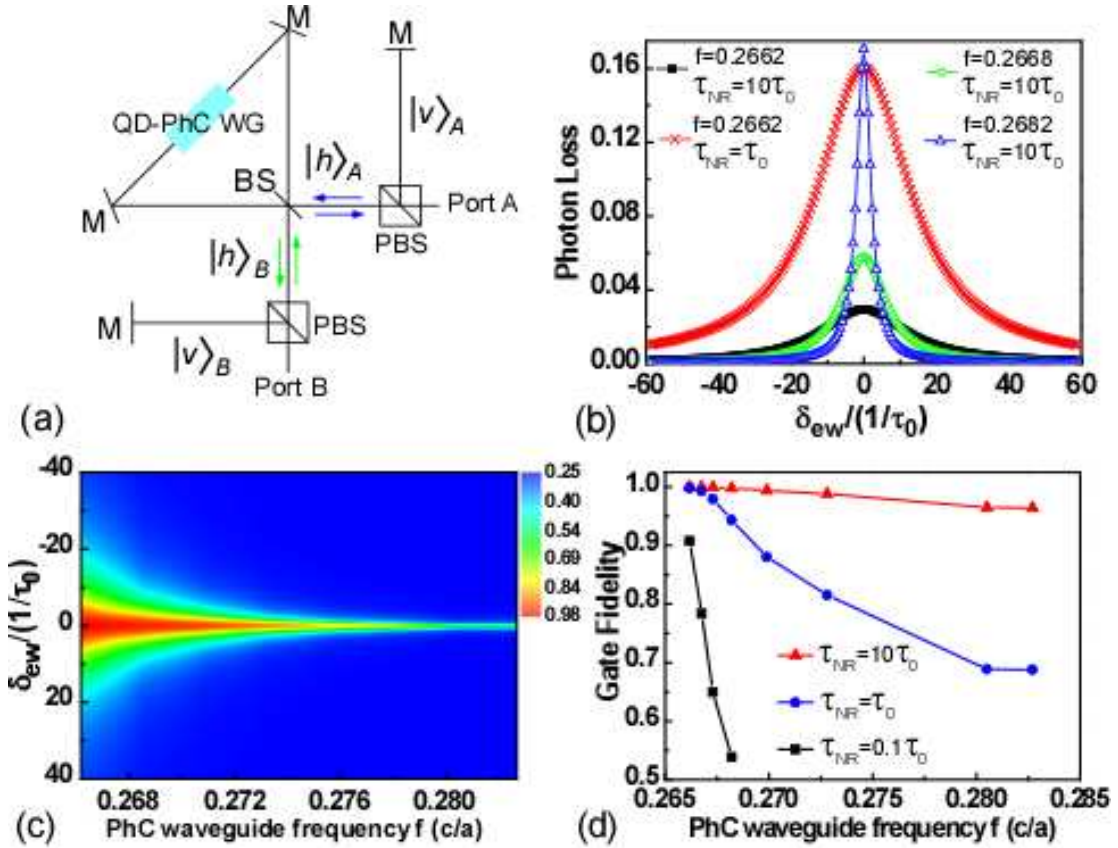


Figure 6.2 (a) Schematic setup of CPF gate with Sagnac loop. Photon A (B) enters from Port A (B) and the h -polarized component (after passing the PBS) interacts with single quantum dot positioned in the PhC waveguide. (b) Gate photon loss as a function of normalized quantum dot detuning frequencies for CPF gate operated at different PhC waveguide frequencies with quantum dot $\tau_{NR} = 10\tau_0$ and $\tau_{NR} = \tau_0$. (c) Gate fidelity for different detuning frequencies and PhC waveguide frequencies ($\tau_{NR} = 10\tau_0$) (d) CPF gate fidelity as a function of normalized PhC waveguide frequencies with quantum dots $\tau_{NR} = 10\tau_0$, $\tau_{NR} = \tau_0$ and $\tau_{NR} = 0.1\tau_0$.

Bibliography

- [1] J.McKeever, A. Boca, A.D.Boozer, R.Miller, J.R.Buck, A.Kuzmich and H.J.Kimble, *Science* **303**, 1992 (2004).
- [2] Y.F.Xiao, J.Gao, X.Yang, R.Bose, G.C.Guo and C.W.Wong, *Appl. Phys. Lett.* **91**, 151105 (2007).
- [3] L.-M. Duan, and H.J.Kimble, *Phys. Rev. Lett.* **92**, 127902 (2004).
- [4] E.Waks and J.Vuckovic, *Phys. Rev. Lett.* **96**, 153601 (2006).
- [5] J. F. McMillan, M. Yu, D.-L. Kwong, C. W. Wong, *Appl. Phys. Lett.* **93**, 251105 (2008).
- [6] D.E.Chang, A.S.Sorensen, E.A.Demler, and M.D.Lukin, *Nature Physics* **3**, 807 (2007).
- [7] V.S.C. Manga Rao and S. Hughes, *Phys. Rev. B* **75**, 205437 (2007); V.S.C. Manga Rao and S. Hughes, *Phys. Rev. Lett.* **99**, 193901 (2007);
- [8] R. Bose, X. Yang, R. Chatterjee, J. Gao, and C. W. Wong, *Appl. Phys. Lett.* **90**, 111117 (2007).
- [9] E.Viasnoff-Schwoob, C.Weisbuch, H.Benisty, S.Olivier, S.Varoutsis, I.Robert-Philip, R.Houdre and C.J.M.Smith, *Phys. Rev. Lett.* **95**, 183901 (2005).
- [10] W.Langbein, P.Borri, U.Woggon, V.Stavarache, D.Reuter and A.D.Wieck, *Phys. Rev. B* **70**, 033301 (2004).
- [11] J.T.Shen and S.Fan, *Opt. Lett.* **30**, 15 (2005).
- [12] Y. Tanaka, J. Upham, T. Nagashima, T. Sugiya, T. Asano, and S. Noda, *Nature Mat.* **6**, 862 (2007).

- [13] R.A.Campos, B.E. A.Saleh and M.C. Teich, Phys. Rev. A **40**, 1371 (1989).
- [14] J.I.Cirac, P.Zoller, H.J.Kimble and M.Mabuchi, Phys. Rev. Lett. **78**, 3221 (1997).
- [15] A.V.Gorshkov, A.Andre, M.Fleischhauer, A.S.Sorensen, and M.D.Lukin, Phys. Rev. Lett. **98**, 123601 (2007).
- [16] A. D. Boozer, A. Boca, R. Miller, T. E. Northup and H. J. Kimble, Phys. Rev. Lett. **98**, 193601 (2007).
- [17] Y. A. Vlasov, M. O. Boyle, H. F. Hamann, and S. J. McNab, Nature **438**, 65 (2005).

Chapter 7

Phase switching through two quantum dots in a slow-light photonic crystal waveguide

7.1 Introduction

Cavity-dipole system has been well discussed in quantum optics and quantum information processing and lots of theory work and experiments have been done in the past 10 years covering topics from enhanced spontaneous emission in weak coupling region to Rabi splitting in strong coupling region, from single photon source to quantum logic gate. A cavity coupled to a dipole can exhibit dipole induced transparency (DIT) [1], which has similar properties to electromagnetically induced transparency in atomic gases system [2]. Using the QD-waveguide system discussed in Chapter 6 which serves as a good broadband integrated platform for light-matter interactions, in this Chapter we present a silicon PhC waveguide system with two low dimensional semiconductor QDs, which can also show DIT phenomenon and dispersive properties without high Q cavity assistance. It makes use of tight confinement and low group velocity of waveguide modes to influence the emission rates of localized QDs. Large optical nonlinearities can be created by a small number of photons, or even a single photon in this system and can be useful for full π phase switching with proper design of a hetero-photonic crystal structure. Photonic crystal waveguide, together with quantum dot, has great potential for the applications from “optical transmission line” to “information processing”.

7.2 Transport property for photonic crystal waveguide embedded with two quantum dots

For standard silicon PhC W1 waveguide (lattice constant $a = 420\text{nm}$), dispersion diagram of fundamental TE-like propagation mode is shown in Figure 7.1(a). A divergent-like LDOS for frequencies lying near the PhC waveguide cut-off is expected with a fundamental propagating waveguide mode. An emitter embedded in a PhC waveguide (at the field maximum of the localized waveguide mode) exhibits a large spontaneous emission enhancement which is proportional to $1/(v_g V_{eff})$. Furthermore, large propagation mode β factor (probability of a photon being emitted into a desired waveguide mode) is obtained throughout a broad propagation spectrum, and $\beta > 0.99$ if normalized frequency of waveguide mode $f_{wg} = a \cdot c / 2\pi\omega_{wg}$ is within 1.5 THz near the cut-off frequency [3]. Figure 7.1(b) shows a schematic diagram of a photonic crystal waveguide with two localized emitters. First we simply consider two-level configuration for the emitters and the states $|1\rangle$ and $|2\rangle$ of emitter A (B) have transition frequency ω_A (ω_B) which can couple to PhC waveguide mode via h -polarization photons (corresponds to waveguide TE mode). We assume transition ω_A (ω_B) is very close to the band edge of the fundamental waveguide mode, and $\omega_{wg} - \omega_{A(B)} \equiv \Delta\omega_{A(B)}$ are very small compared to the slow light bandwidth. $\kappa_A \approx \kappa_B = \kappa = 1/\sqrt{2\tau_{SE}}$ is the coupling coefficient between the emitter transition and the waveguide mode. We denote σ_{A-}^{12} (σ_{B-}^{12}) as the lowering operator for the emitter A (B), and the Heisenberg operator equations are given by

$$\begin{aligned}
\frac{d\sigma_{A-}^{12}}{dt} &= -\frac{1}{2\tau_A}\sigma_{A-}^{12} + i\Delta\omega_A\sigma_{A-}^{12} + \kappa a_{in} + \kappa b_{in} \\
\frac{d\sigma_{B-}^{12}}{dt} &= -\frac{1}{2\tau_B}\sigma_{B-}^{12} + i\Delta\omega_B\sigma_{B-}^{12} + \kappa a_{in} + \kappa b_{in}
\end{aligned} \tag{7.1}$$

where a_{in} (b_{in}) and a_{out} (b_{out}) are the field operators for the flux of the waveguide input and output port. Both emitters have the decay rate $1/\tau_{A(B)} = 1/\tau_{SE} + 1/\tau_{NR} + 1/\tau'$ in which $1/\tau_{SE} = PF/\tau_0$ is the emitter's modified spontaneous emission rate in PhC waveguide, $1/\tau_{NR}$ is the nonradiative decay rate and $1/\tau'$ is related to the spontaneous emission into a continuum of radiation and/or leaky modes. We define the amplitude T and phase ϕ_t of the transmission coefficient by $t = a_{out}/a_{in} = \sqrt{T}e^{i\phi_t}$. We consider QD $\tau_0 = 1\text{ns}$ [1] and nonradiative decay could be sub GHz at low temperature [4]. Figure 7.1(c) shows the transmittance and phase (normalized by π) as a function of $\Delta\omega = \omega_{wg} - (\omega_A + \omega_B)/2$ when the transition difference $|\omega_A - \omega_B| \cdot \tau_0 = 30$. We use $PF = 28.5$, $\beta = 0.997$ [3] in the calculation because f_{wg} and emitter frequencies are very close to the typical slow group velocity region. Different from the case in which photon is completely reflected by a single emitter in surface-plasmons nanowire [5] or photonic crystal waveguide [6-7] discussed in Chapter 6, dipole induced transparency can be observed if the two QDs are properly located in the photonic crystal waveguide with distance $L = 4a$ or its multiples. The appearance of the peak is analogous to the atomic vapor system [2] and cavity-dipole system [1]. Similar concept can be found in [8], and it turns out photonic crystal waveguide is a promising platform for one-dimensional circuit quantum

electrodynamics system. The transparency peak width is adjustable via tuning the QD frequencies or QD decay rates. Although the propagation loss of the slow-light waveguide mode is relatively large as $\sim 500\text{dB/cm}$ [9], it is still neglectable between two QDs because $L = 4a$ is a very short distance, and even true for the whole waveguide which be compacted within $\sim 30\ \mu\text{m}$ length.

7.3 Construction schemes for full π phase switching

We now explore the dispersive and nonlinear properties of a system shown in Figure 7.2, which consisting of an in-plane hetero-photonic crystal structure and two three-level emitters, to realize a full π phase switching. The individual regions PC_1 and PC_2 have different lattice constants (a_1 and a_2 respectively). We design the lattice constants to realize that photons with wavelengths lying near the PC_1 waveguide cut-off cannot propagate along the waveguide in PC_2 [10]. The hetero-interface becomes a perfect mirror and only introduces a phase change φ on the reflection so that $b_{\text{in}} = a_{\text{out}} \cdot e^{i(2k \cdot d + \varphi)}$. The states $|1\rangle$, $|2\rangle$ and $|3\rangle$ in emitter A (B) have transition frequency ω_A (ω_B) and ν_A (ν_B) as shown in Figure 7.2, and all the transitions can couple to PhC waveguide mode via h -polarization photons (corresponds to waveguide TE mode). We define the amplitude and phase of the reflection coefficient by $r = b_{\text{out}}/a_{\text{in}} = \sqrt{R}e^{i\phi_r}$ and design the geometry so that $2k \cdot d + \varphi = 2\pi$. Similar treatments and parameters as the above calculation give us Figure 7.3 (a) which shows the reflectance R and phase ϕ_r (normalized by π). Near 90% of the input is reflected by

the system with zero phase change at central frequency, which is opposite to the case in which on-resonant photon is reflected by a bare cavity or a single emitter in waveguide with π phase change. Phase of the reflection is highly dispersive near $\Delta\omega = 0$, and quickly changes from 0 to π at a detuning of $\Delta\omega = 0.014 \text{ THZ}$. The slope of ϕ_r gives the group delay a pulse experiences from system reflection in Figure 7.3(a) (bottom curve), and the second derivative of ϕ_r near zero detuning vanishes ensuring that the reflected pulse preserve its shape. Figure 7.3(b) and (c) discuss about the effect of QD properties on the reflection and dispersion. When the nonradiative rate is even two times larger than $1/\tau_0$, only the reflection drops from 0.9 to 0.4 but the phase dispersion keeps unchanged. When the frequency difference between two QDs increases to $50\tau_0$, the reflection becomes higher but the phase dispersion becomes more linear and it requires more frequency shifting to change phase from zero to π . If the design parameters in the actual device vary from the idea values, Figure 7.3(d) and (e) show the reflectance and phase when the separation distance L is 12nm larger than $4a$ and when $2k \cdot d + \phi$ is 10% larger than 2π respectively. At zero detuning, the phase change is no longer zero anymore and the whole curves shift to the left and right respectively.

The sharp dispersion feature of the reflection phase allows the possibility to achieve full π phase switching by shifting the dispersion curve by a very small amount photons. Assume the input field has two frequency components, one at ω_{wg} which drives $\sigma_{A(B)-}^{12}$ and the other at $\nu_A + \Delta$ which off-resonantly drives σ_{A-}^{23} to create a Stark

shift on the first quantum dot A. In the case of QD, we can use the single exciton and biexciton transition for $|1\rangle - |2\rangle$ and $|2\rangle - |3\rangle$ transitions. It is reasonable to assume that $\nu_A + \Delta$ is also within the slow group velocity region and $\kappa_{23} = \kappa$ for quantum dot A.

Detuning of $|1\rangle - |2\rangle$ transition in the presence of the Stark field $\nu_A + \Delta$ can be

expressed as $\delta_A = \frac{i2\kappa_{23}^2 (a_{in(\nu+\Delta)})^2 / h(\nu + \Delta)}{i\Delta + 1/\tau_3} = \frac{i2\kappa_{23}^2 N/T}{i\Delta + 1/\tau_3}$ [11], where N is the

number of photons absorbed and T is the pulse duration of the Stark field. The real component of δ gives the optical Stark shift to the first quantum dot, while the imaginary component represents the loss. Figure 7.4 shows the reflectance and phase when $\Delta = 0.4 THZ$ (larger than $1/\tau_3$), $T = 40ps$ (shorter than the modified spontaneous emission lifetime) and $\langle N \rangle = 5$. Compared to the case without any Stark field, near π phase shift can be achieved by inputting the system with several photons at the Stark field frequency and reflecting the other pulse on resonance with the QD. This is already orders of magnitude smaller than conventional methods. If one can control the frequency detuning between the two QDs to be even smaller to get sharper dispersion, only one photon on average from the waveguide input is enough to achieve this phase shift. Compared to the dipole-cavity system, there is always a trade-off between coupling efficiency and loaded Q so that we need a lot of photons as input to load 1-10 photons of Stark field into the high Q cavity [11]. Large optical confinement and slow light waveguide mode in photonic crystal waveguide provide large interaction between QDs and the propagation mode, which generates very strong optical

nonlinearities to cause Stark shift. Also it shows that we can drive the system on resonance but without suffering from large loss from the absorption of the quantum dots, and the reflection is always 80% or more.

7.4 Conclusion

In summary, we propose a system which consisting of two QDs located in a photonic crystal waveguide to be useful in quantum optics and quantum computation. It possesses large dispersion and nonlinearities, and can be designed to realize full π phase switching with only several Stark field photons needed. Strong optical confinement and low group velocity in photonic crystal waveguide contributes to the high reflectance and sharp dispersion. Different with other cavity-assisted schemes, excitation and extraction can be extremely efficient and chip-scale integration is possible. Also it is much easier to realize the frequency match condition between the central frequency of two QDs and waveguide mode because photonic crystal waveguide slow-light mode has relatively broad frequency region than high Q cavities. All these advantages show QD-photonic crystal waveguide system is very promising to be a critical component in quantum information processing.

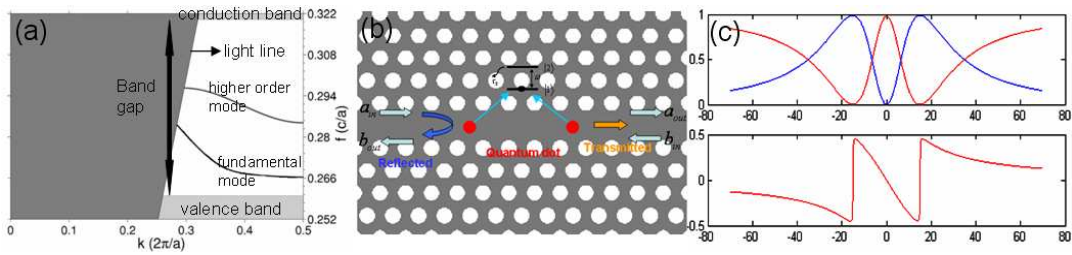


Figure 7.1 (a) PhC waveguide band structure within the TE-like band gap. Both fundamental and higher order modes are shown. Structure parameters: $r=0.275a$, $h=0.5a$, $\epsilon=12$ and $a=420\text{nm}$. (b) Schematic diagram of incident beam interacts with two near resonant QDs. (c) Transmittance (red in upper (c)), Reflectance (blue in upper (c)) and phase of the transmitted beam (bottom (c)) as a function of input frequencies. $|\omega_A - \omega_B| \cdot \tau_0 = 30$, $\tau_0 = 1\text{ns}$ and distance between two QDs $L = 4a$.

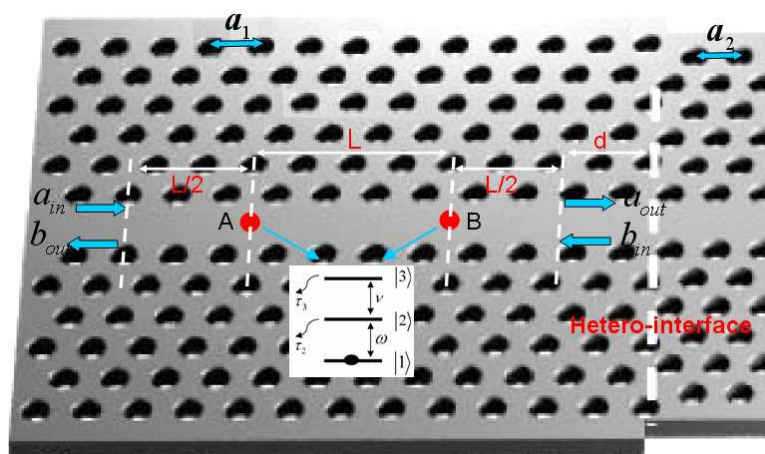


Figure 7.2 Schematic diagram for full π phase switching based on an in-plane heterophotonic crystal structure and two three-level QDs. Lattice constants in different photonic crystal region is a_1 and a_2 . The distance between the hetero-interface and quantum dot B is $L/2+d$ and the phase introduced by reflection at the interface is φ , which satisfy $2k \cdot d + \varphi = 2\pi$.

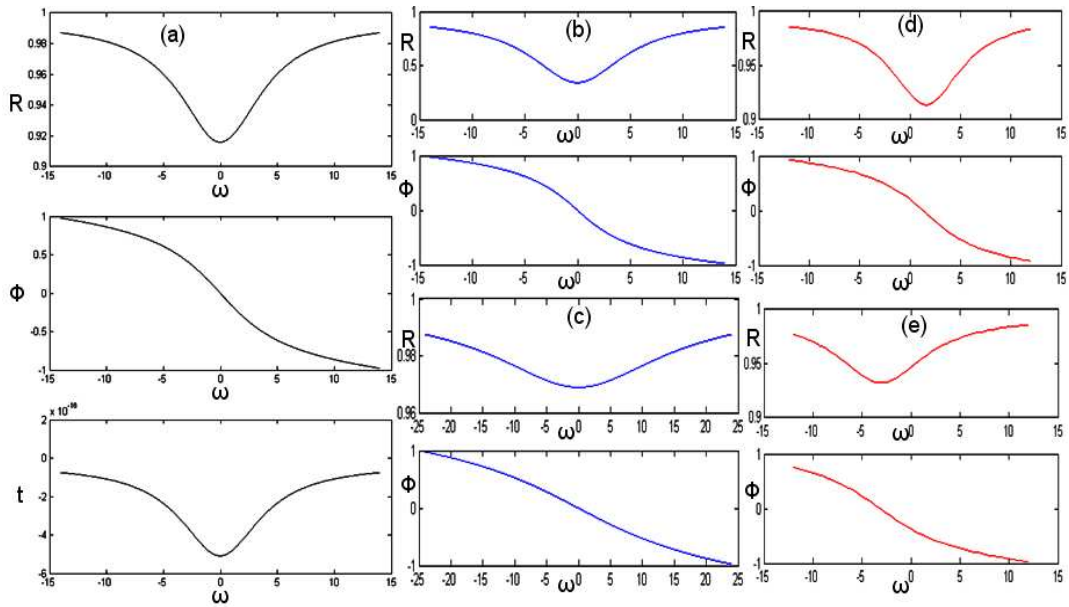


Figure 7.3 (a) Reflectance, phase and group delay for $\tau_0 = 1\text{ns}$, $\tau_{\text{NR}} = 10\tau_0$, $|\omega_A - \omega_B| \cdot \tau_0 = 30$, $2k \cdot d + \phi = 2\pi$ and $L = 4a$. Reflectance and phase when (b) $\tau_{\text{NR}} = 0.5\tau_0$ (c) $|\omega_A - \omega_B| \cdot \tau_0 = 50$ (d) $2k \cdot d + \phi = 2.2\pi$ (e) $L = 4.02a$. All the other parameters keep the same as (a) for each case.

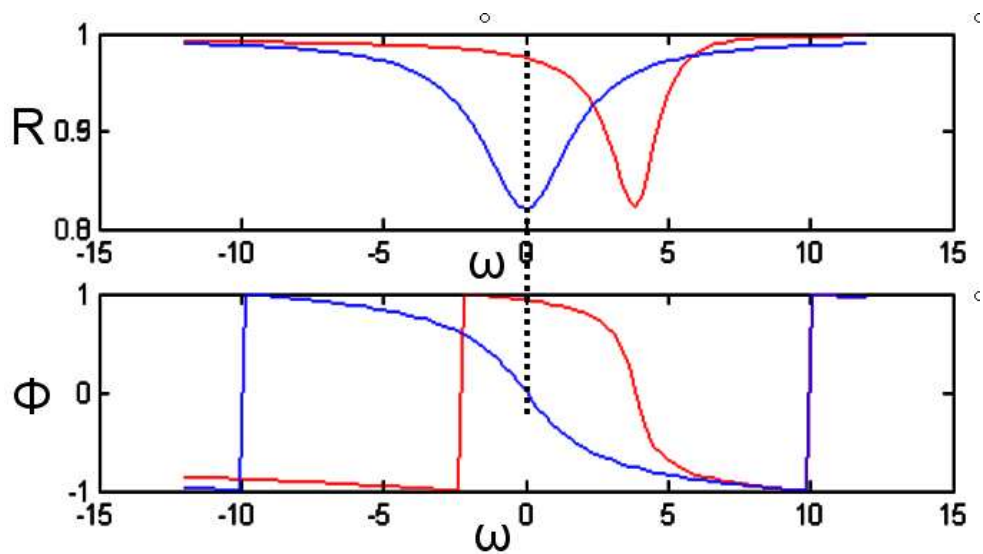


Figure 7.4 Reflection and phase when there is Stark field (red curve) and no Stark field (blue curve). $|\omega_A - \omega_B| \cdot \tau_0 = 20$, $\Delta = 0.4$ THZ, $T = 40$ ps and $N=5$.

Bibliography

- [1] E.Waks and J.Vuckovic, Phys. Rev. Lett. **96**, 153601 (2006).
- [2] H.Schmidt and A.Imamoglu, Opt. Lett. **21**, 1936 (1996)
- [3] V.S.C.Manga Rao and S.Hughes, Phys. Rev. B **75**, 205437 (2007).
- [4] W.Langbein, P.Borri, U.Woggon, V.Stavarache, D.Reuter and A.D.Wieck, Phys. Rev. B **70**, 033301 (2004).
- [5] D.E.Chang, A.S.Sorensen, E.A.Demler, and M.D.Lukin, Nature Physics. **3**, 807 (2007).
- [6] J.Gao, F.Sun and C.W.Wong, Appl. Phys. Lett. **93**, 151108 (2008).
- [7] J.T.Shen, and S.Fan, Opt. Lett. **30**, 15 (2005).
- [8] J.T.Shen. M.L.Povinelli, S.Sandhu and S.Fan, Phys. Rev. B **75**, 035320 (2007).
- [9] E.Kuramochi, M.Notomi, S.Hughes, A.Shinya, T.Watanabe and L.Ramunno, Phys. Rev. B **72**,161318 (2005)
- [10] Y.Akahane, T.Asano, H.Takano, B.Song, Y.Takana and S.Noda, Opt. Express **13**,7 (2005)
- [11] E.Waks and J.Vuckovic, Phys. Rev. A **73**,041803(R) (2006)

Chapter 8

Summary and future outlook

8.1 Summary: chip-scale photonic devices for light-matter interactions and quantum information processing

In this thesis, chip-scale photonic devices such as whispering gallery mode microcavities, photonic crystal nanocavities and slow-light photonic crystal waveguide are designed, fabricated and characterized. The strong light localization and long photon lifetimes in these devices can enhance the light-matter interaction significantly, presenting many opportunities to realize new functionalities in integrated nanophotonic circuits. Particularly with semiconductor quantum dots, exciton-photon coupling and quantum logic gate are studied as examples for the applications of chip-scale photonic devices in cavity electrodynamics and quantum information processing. They are the building blocks for the future high-density “quantum photonic circuits”.

High quality factor (Q), subwavelength mode volume (V) and controllable radiation directionality are the major properties for optical cavities designs. Engineered control of radiation directionality in asymmetric resonant cavities is discussed in Chapter 2. High quality factor of 10^4 and small effective mode volume ~ 0.02 cubic wavelengths for air-slot mode-gap photonic crystal cavities is demonstrated in Chapter 3. Furthermore in Chapter 4, exciton-photon coupling between ensemble PbS quantum dots and these air-slot mode-gap photonic crystal cavities are examined in weak coupling regime with photoluminescence enhancement and modified spontaneous emission rate. In order to move into studies at single quantum dot level, in Chapter 5 subpoisson photon statistics from a single InAs quantum dot emission is

presented and strong coupling between single quantum dot exciton line and photonic crystal waveguide localized mode is demonstrated experimentally and theoretically analyzed with master equations. Besides high Q photonic crystal cavities, slow-light waveguide with the excellent physical integration is a great implementation platform for realizing future large-scale solid-state quantum computation. In Chapter 6 and 7, implementation schemes to realize quantum controlled phase gate and phase switching through quantum dots embedded in a photonic crystal waveguide are proposed.

8.2 Future outlook: nanoscale plasmonic devices for light-matter interactions

High Q optical cavities and slow-light waveguides studied in this thesis are photonic devices with light confined in dielectric materials such as silicon or GaAs. When we further explore from chip-scale devices with size \sim few to tens of μm to nanoscale, surface plasmon polaritons (SPPs), which confines electromagnetic waves propagating along a metal-dielectric interface by the collective optical excitations of the free electrons, brings new capabilities in confining optical field to deep subwavelength scale and eliminating the restriction on the size of optical nanocavities [1, 2]. Since SPPs supports high wave vectors and therefore ultrashort wavelengths, plasmonic nanocavities having subwavelength mode volumes can be designed to realize high Q/V ratio although the Q factor is limited by the metal loss. For example, plasmonic microdisks resonators [3], metallic Fabry-Pérot resonators [4], metallic-coated cavities

[5, 6], and hybrid plasmonic crystal nanocavities [7] have been proposed and studied recently. The strongly localized optical energy in these resonant plasmonic nanostructures provides many opportunities for realizing active functionalities at nanoscale, such as label-free biosensors [8], enhanced light-matter interactions [9], plasmonic nanolasers [10] and high efficiency solar cells [11].

The concentrated optical near fields in resonant plasmonic nanostructures can increase the photon density of states and the spontaneous emission rate of emitters, and lead to the enhancement of light emission by emitter-surface plasmon coupling, which provides an effective way for developing efficient solid-state light sources such as LEDs and nanolasers. In quantum regime, the emission from a single nanoemitter, such as semiconductor quantum dot, diamond nitrogen-vacancy (NV) center or photoluminescence molecule, can couple to quantized surface plasmons directly for realizing quantum plasmonic devices, for example, single photon source, single-photon switching and transistor, with consumed energy at single photon level.

Bibliography

- [1] W. L. Barnes, A. Dereux, and T. W. Ebbesen, Surface plasmon subwavelength optics, *Nature* **424**, 824 - 830 (2003).
- [2] J. A. Schuller, E. S. Barnard, W. Cai, Y. C. Jun, J. S. White, and M. L. Brongersma, Plasmonics for extreme light concentration and manipulation, *Nature Materials* **9**, 193 (2010).
- [3] B. Min, E. Ostby, V. Sorger, E. Ulin-Avila, L. Yang, X. Zhang, and K. Vahala, High-Q surface-plasmon-polariton whispering-gallery microcavity, *Nature* **457**, 455-458 (2009).
- [4] V. J. Sorger, R. F. Oulton, J. Yao, G. Bartal, and X. Zhang, Plasmonic Fabry-Pérot nanocavity, *Nano Letters* **9**, 3489 (2009).
- [5] M. T. Hill, *et al.*, Lasing in metallic-coated nanocavities, *Nat. Photon.* **1**, 589-594 (2007).
- [6] Nezhad, M.P. et al. Room-temperature subwavelength metallo-dielectric lasers. *Nat. Photon.* **4**, 395-399 (2010).
- [7] X. Yang, A. Ishikawa, X. Yin, and X. Zhang, Hybrid photonic-plasmonic crystal nanocavities, *ACS Nano*, **5**, 2831-2838 (2011).
- [8] C. Wu, *et al.*, Fano-resonant asymmetric metamaterials for ultrasensitive spectroscopy and identification of molecular monolayers, *Nature Materials* **11**, 69–75 (2012).
- [9] J. T. Choy, *et al.*, Enhanced single-photon emission from a diamond–silver aperture, *Nature Photonics* **5**, 738–743 (2011).
- [10] R. F. Oulton *et al.*, Plasmon lasers at deep subwavelength scale, *Nature* **461**, 629-632 (2009).
- [11] H. A. Atwater and A. Polman, Plasmonics for improved photovoltaic devices, *Nature Materials* **9**, 205–213 (2010).